



UNIVERSITY
OF TWENTE.

Analysis of Short-Circuit Transients in the LHC Main Dipole Circuit and Development of an Automated Analysis Algorithm

Bachelor Thesis

Akrivi Liakopoulou

Supervisors:

Prof. Dr. J. Schmitz, University of Twente

Dr. Ir. C. Salm, University of Twente

Dr. E. Ravaioli, CERN

Geneva, Switzerland

March 2019

CONTENTS

List of Abbreviations

Abstract

1	Introduction	1
1.1	Project Introduction and Motivation	1
1.1.1	Research Questions	2
1.1.2	Thesis Structure	3
2	LHC Main Dipole Circuit Modeling	4
2.1	Introduction to the LHC Main Dipole Circuit	4
2.2	Superconducting Magnets and Quench	5
2.3	Modeling the LHC Main Dipole Circuit	7
2.3.1	Modeling Background	7
2.3.2	Equivalent Model of the LHC Main Dipole Circuit and Magnets	8
2.3.3	Circuit Behaviour Following Fast Power Abort	9
3	Worst-Case Analysis Of Short-Circuit Transients	14
3.1	Modeling Short Circuit to Ground	14
3.1.1	Circuit Behaviour Following Single Short Circuit to Ground	16
3.2	Modeling Circuit Fuse Blow-Up Behaviour	20
3.3	Circuit Behaviour Following Fuse Blow-Up and Identification of Worst-Cases	24
4	Short Circuit Algorithm	32

4.1	Simplifying the LHC Main Dipole Equivalent Electrical Circuit	33
4.2	Analytical Solution of Reduced Equivalent Circuit Model	35
4.3	Design of Short Circuit Algorithm	41
4.4	Testing of Algorithm And Results	47
4.5	Discussion and Future Work	56
5	Conclusion	57
A	Appendix	62
A.1	Wye-Delta Transform	62
A.2	LHC Magnet Crate Layout	64
A.3	Complete Expressions of Circuit Currents Analytical Solutions	65
A.4	GitLab Repository	65

LIST OF ABBREVIATIONS

Notation	Description
ALICE	A Large Ion Collider Experiment.
ATLAS	A Toroidal LHC ApparatuS.
CERN	Conseil Européen pour la Recherche Nucléaire.
CMS	Compact Muon Solenoid.
EE	Energy Extraction.
EE1	Energy Extraction 1.
EE2	Energy Extraction 2.
FPA	Fast Power Abort.
LHC	Large Hadron Collider.
LHCb	Large Hadron Collider-beauty.
STEAM	Simulation of Transient Effects in Accelerator Magnets.
TE-MPE-PE	Technology-Machine Protection and Electrical Integrity-Performance Evaluation.

Abstract

The Large Hadron Collider (LHC) spreads over a total distance of 26.7 km and comprises 8 sectors. In each sector there is one main dipole circuit, where 154 superconducting dipole magnets are connected in series. Since 2007, there have been 19 occurrences of short-to-ground faults in the superconducting LHC main dipole circuits, making their analysis and understanding necessary for the efficient operation of the accelerator.

After the occurrence and detection of a short to ground, a fast power abort is triggered and the current in the circuit starts decaying semi-exponentially from a maximum value of 11.85 kA to zero, with a time constant of about 103 s. In the case where a short to ground exists in the circuit, the current flows through the fuse that is present in the grounding subcircuit. Depending on the value of its thermal load, the fuse first enters a pre-arcing region where it starts intermittently blowing up, until the blow-up threshold is reached, after which the fuse stays definitively blown. A simulation scheme utilising a common interface between *PSpice* and *MATLAB* is proposed in order to simulate the blow-up behaviour of the fuse and to consequently increase the accuracy of the circuit model. A parametric analysis of the short to ground parameters is performed and a better understanding of the circuit's behaviour under different conditions is achieved. The worst-case voltage to ground values in the LHC main dipole circuit are identified for the case where the intermittent behaviour of the fuse is included in the model and a comparison is given with the values obtained when the blow-up behaviour of the fuse is not modelled.

The appearance of a fault in the circuit requires the immediate switch-off of the machine, so that experts can visit the site and resolve it. Due to the large circumference of the LHC, searching for the fault's position without any prior knowledge requires a large amount of time, increasing the need for an automated solution, which is able to provide information regarding the short circuit, to be created.

With a better understanding of the circuit behaviour after the occurrence of a short to ground event, stemming from the first part of the thesis, an equivalent circuit model of the LHC main dipole circuit for short transients, that can be solved analytically, is derived. An algorithm is proposed to take advantage of the reduced time needed to solve the system analytically, when compared to a numerical approach. The algorithm is able to provide information regarding the short location as well as identify the range of values in which the short resistance belongs. This greatly reduces the time needed by an expert to analyse a short-circuit event in the LHC main dipole circuit. The algorithm is tested using measured data from a real short-circuit event. Due to the fact that the simplified circuit model consists only of inductive and resistive elements, the algorithm is flexible and can also be applied to different accelerator magnet circuits.

CHAPTER 1

INTRODUCTION

1.1 Project Introduction and Motivation

CERN, the European Organization for Nuclear Research, operates since 1954 in Geneva. Alongside a plethora of contributions to science, the organization is also responsible for building and operating multiple accelerators, with the LHC reserving the title of the world's largest machine and particle collider [1].

As is the case in all electrical systems, abnormal conditions commonly characterized as faults disturb the normal operation of the system and can cause damage to its electrical sub-parts. In the case of the LHC circuits, which include highly expensive superconducting magnets and store energy in the range of GJ [2], electrical faults can put equipment at risk or cause a temporary shutdown of the accelerator, until all problems have been resolved. Hence, it goes without saying that it is of utmost importance to ensure the protection of a machine operating under such high ratings as the LHC.

Despite a large amount of research preceding the initial startup of the accelerator in 2008, there have been in total 19 occurrences of earth failures in the LHC main dipole circuit. Mentioning the incident of 2008 at this point, can help clearly outline the effects of a fault appearance in the circuit. The specified fault occurred during the ramp-up of the main dipole circuit of the LHC in *Sector 34* with the cause identified as the appearance of a resistive region in the electrical bus between a dipole and quadrupole magnet [3], that was not detected in time. The electrical arc that appeared, punctured the enclosure of the helium, which then started spreading to the insulation vacuum of the cryostat. This consequently resulted in a pressure rise which in turn caused significant displacements of the magnet interconnections, as shown in figure 1.1. After a thorough investigation, the substitution of 29 superconducting magnets from the tunnel was deemed necessary [4].

With the installation of various sensors and specialized equipment in certain areas of the circuit, constant monitoring can be achieved during the LHC active operation peri-

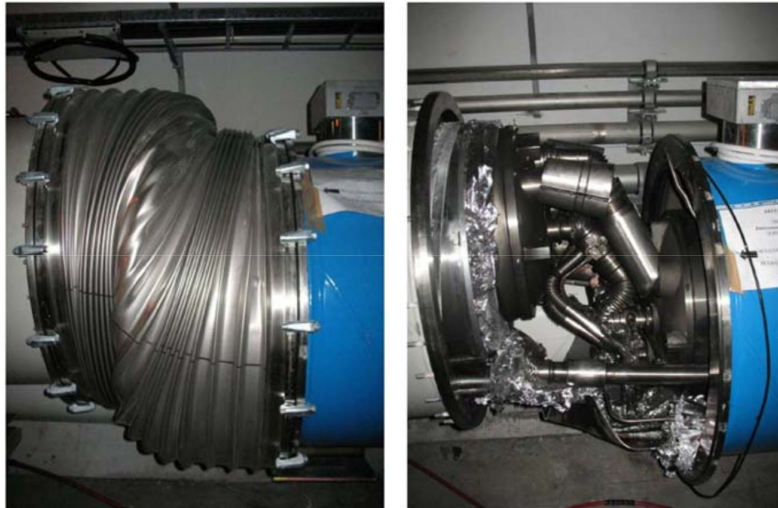


Figure 1.1: Visible damage on an LHC magnet interconnection after the occurrence of the 2008 incident [4].

ods. This means that in case a fault occurs in the circuit, it will be identified quickly and the protection systems will be triggered so that its effect can be confined. Following the event, if necessary, a team will visit the tunnel in order to perform potential equipment replacements, which implies that certain information about the fault, such as its position along the magnet chain, needs to be known. The process of obtaining information regarding the fault currently requires accessing the measured data of the time window that includes the time the fault occurred from a database, followed by thorough analysis so that conclusions can be drawn regarding the incident. Therefore, it becomes obvious that experts with knowledge of the LHC circuit and its behaviour need to perform the required analysis of the measured signals in order to provide more information about the event. As a consequence, following the appearance of a short in the circuit, it is possible that several working hours can be dedicated before useful conclusions can be drawn.

1.1.1 Research Questions

The main objectives of this thesis is to analyse the transients following the occurrence of a fault and more specifically a single short circuit to ground in the LHC main dipole circuit, assess worst cases and develop an algorithm that can be used to automate the process of providing fault information. The goal of the algorithm will be to draw conclusions regarding the short significantly faster, compared to the time that an expert would require when using existing circuit models and numerical simulations. While working towards a solution, it is essential to obtain a better understanding of the circuit behaviour following the occurrence of a short to ground and for this reason, a method to more accurately model the blow-up behaviour of the fuse in the circuit is analysed and presented. The research questions to be addressed are summarized below.

1. What worst cases can be identified when a single short to ground appears in the circuit? Can the model of the LHC be improved by including the blow-up behaviour

of the fuse present in the circuit's earthing point?

2. How much can the electrical equivalent circuit model of the LHC main dipole circuit be simplified, while still providing useful information about the circuit behaviour during a fault?
3. Is it possible to construct an algorithm to provide information concerning a fault that occurred in the LHC main dipole circuit faster than a mediating expert working with numerical simulations? What level of confidence does such an algorithm have?

1.1.2 Thesis Structure

Although this work aims to answer more than one research questions, the fact that they are closely related allows for results drawn in the first part of the thesis to be used in later sections. The structure implemented in the thesis is outlined next. The first part focuses on how the circuit behaves under the occurrence of a fault, while in the second part the steps taken towards automating the procedure of providing the details of a potential fault as well as the proposed algorithm are presented. More specifically :

In chapter 2, a general introduction to the LHC main dipole circuit is given and the design choices for the main dipole equivalent model are briefly discussed. This aims to get readers without previous knowledge of the LHC main dipole circuit familiar with the various models and circuit components analyzed in the thesis, making hence the results accessible to a wider audience.

In chapter 3, the chosen method for modeling a single short to ground, as well as a simulation scheme that models the blow-up behaviour of the circuit fuse are outlined. The simulation results for different parameters of the short are also presented and discussed. From the simulation data, the worst cases, in terms of the peak voltage to ground achieved in the LHC main dipole circuit, are identified and the conditions under which they occur are outlined.

In chapter 4, the schematic of the LHC main dipole circuit is reduced to an equivalent, that models the behaviour of the circuit when a short to ground has occurred. An algorithm is proposed which is based on the analytical solution of the circuit. It can provide information on a single short to ground starting from the measured data of the event. The accuracy of the algorithm is tested using measured signals from the event of December 8th 2016, when a single short to ground occurred in the circuit. Results and further applications are also discussed.

CHAPTER 2

LHC MAIN DIPOLE CIRCUIT MODELING

2.1 Introduction to the LHC Main Dipole Circuit

The LHC accelerator located at CERN has a perimeter of about 27 km and is the largest particle accelerator in the world crossing the border of two countries, namely France and Switzerland. Experiments are being carried out in the institute with the goal of gaining a better understanding of particle physics and the universe. A visual representation of the accelerator is shown in figure 2.1, where special attention can be drawn to its eight sectors, with names ranging from *Sector 12* to *Sector 81*.

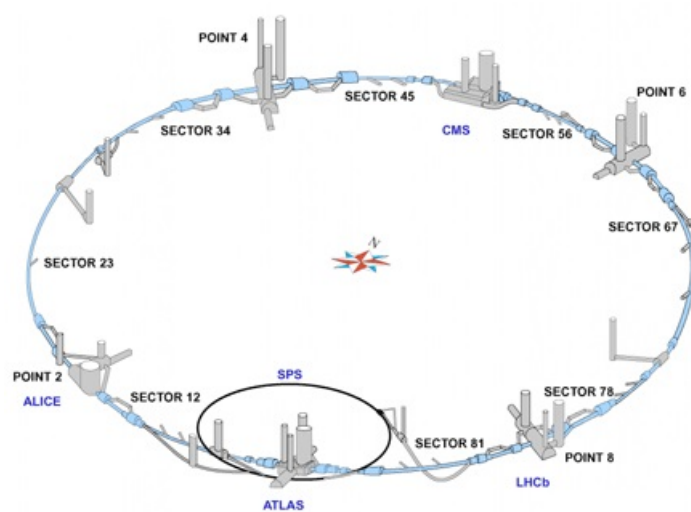


Figure 2.1: Graphical representation of the LHC layout [5].

One of the main purposes of the accelerator is to allow particle beams to circulate in a stable orbit, by keeping the particles' trajectory well defined and aligned at high

levels of precision. It is also responsible for colliding the particle beams and detecting secondary particles after the collisions. Since the beam is charged, it is essential to have control over it, so that damage to the magnets is avoided and the points where the collisions are allowed to happen remain well defined. A total of about 6000 magnets are necessary for the operation of the accelerator. Among them 1232 are main dipole or main bending magnets (MB), which take up more than 2/3 of the accelerator's tunnel, 392 are main quadrupole magnets, with the rest being other magnet types such as insertion quadrupole magnets and corrector magnets.

Each proton beam circulating in the accelerator reaches a maximum energy of 3.5 TeV and collisions take place at twice this energy level for approximately 10 hours. Figure 2.1 also includes the four largest experiments located along the circumference of the accelerator, namely [ATLAS](#), [ALICE](#), [CMS](#) and [LHCb](#). These are the locations of the caverns containing either general purpose or specialised detectors, which aim to collect information from the particle collisions that occur at these points [6].

2.2 Superconducting Magnets and Quench

Following the laws of electromagnetism for the trajectory of the beam, the boundaries of the circumference where a beam can circulate under the existence of a constant magnetic field are defined by its energy as well as the strength of the magnetic field. The two variables are proportional and their relationship can be written as $E \propto Br$, where E is the collision energy, B the dipole magnetic field and r the radius of the accelerator. Under the existence of a constant magnetic field, this means that in order for the beam energy to reach higher values, the circumference of the accelerator would also have to be increased. Since this is not possible due to the fixed size of the tunnel where the accelerator is located at, it follows that the desired energy value can only be reached by increasing the strength of the magnetic field. A way to achieve this is to allow more current to pass through the magnets. In order to ensure magnet compactness, while at the same time keeping operating costs to a minimum, the phenomenon of superconductivity can be exploited. Materials that are superconductive at cryogenic temperatures, allow current to flow through them without any resistance and hence dissipate no energy [7].

This is therefore the reason why some of the LHC ordinary electromagnets have been replaced by superconducting ones of different types, depending on their role and position in the accelerator. A large amount of studies exist on the development of the superconducting magnets and an extensive analysis of all the design choices is presented in the LHC Design Report [8]. For this reason, only a short reference to the main bending superconducting dipole magnets, that will be included in the simulations and models discussed in the thesis, is provided in this chapter.

The magnets consist of two apertures powered in series, which confine the space where the beams are allowed to circulate during operation. The nominal current specified during the design of the magnets is equal to 11.85 kA, while the nominal field at the bore reaches a value of 8.3 T. The two apertures are surrounded by a non-magnetic collar

Table 2.1: Parameters of LHC Main Dipole Magnet [8].

Parameter	Value	Unit
Nominal field (7 TeV beam energy)	8.33	T
Current at nominal field	11850	A
Inductance at nominal field	98.7×10^{-3}	H
Stored energy at nominal field (both apertures)	6.93	MJ
Operating Temperature	1.9	K
Cold mass length	15.18	m
Total mass	27.5	t

made of stainless steel, capable of handling the stress and forces acting on the coil during operation, while maintaining the desired coil geometry. The iron yoke surrounds the two apertures as well as the collar and aims to achieve magnetic shielding by reducing the value of the magnetic field beyond a certain distance from the magnet's aperture. A six block geometry is chosen for the construction of the dipole coils, consisting of layers further split into blocks of conductors [9]. From a construction perspective, each of the 1232 main dipole magnets of the LHC main dipole circuit has a curvature of ≈ 9 mm so that when placed in series, the circular shape of the accelerator can be achieved. These superconducting magnets are made of *NbTi* strands arranged in a Rutherford cable [10]. *NbTi*, a type II superconductor, has a critical temperature of 9.2 K, meaning that it loses all its electrical resistance when cooled down to temperatures below this value. Through the cryogenic system installed in the circuit, liquid helium can be cooled down to temperatures of 1.9 K, where its superfluid properties appear and hence sufficient margin is achieved with respect to the normal state [11]. The main magnet parameters are presented in table 2.1 and a complete analysis of the design is outlined in [8].

A quench is defined as the abrupt loss of the superconducting state in a region of the coil. With a specific part of the coil switching to the normal state and current in the order of kA flowing through it, the stored energy converted into heat can cause damage if the quench is not detected in time. For this reason, a large amount of research has been dedicated to the design of quench protection systems [12, 13], with the quench heaters and cold by-pass diodes being the two choices currently installed in the main dipole circuit. Additionally, a quench detection system *QDS* consisting of two subsystems, namely *iQPS* and *nQPS*, is in place in order to detect the occurrence of a quench in the main dipole circuit. These systems are triggered when the values of the signals they monitor exceed a certain threshold, with the former monitoring the differential aperture voltage of the magnets and the latter the voltage over each magnet [14]. The collection and storing of the signals from the two systems is organised by the Post-Mortem system [15], from where signals with specified timestamps can be queried. These systems do not store the signal values in the database continuously, but only after they have been triggered and only for the magnets that quenched.

To better understand the behaviour of a magnet during a quench, the measured

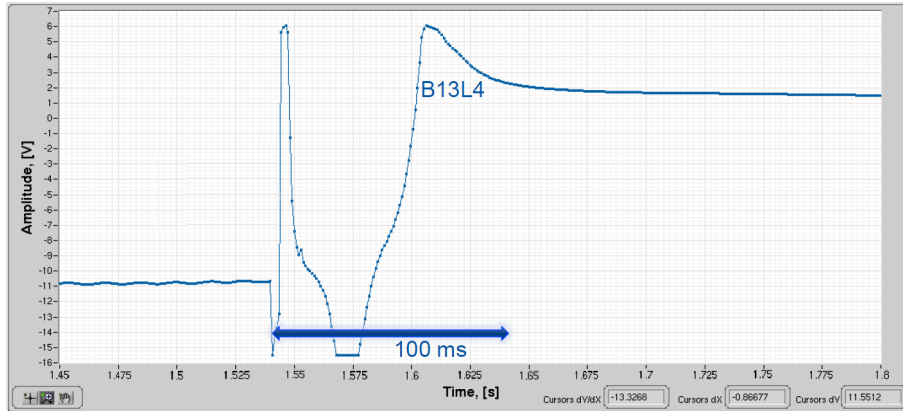


Figure 2.2: Measured voltage over magnet B13L4 showing the superconducting magnet’s quenching behaviour. First a short to ground occurs around 1.54s with the quench following at the time of about 1.58s. The voltage first reaches a value of 6 V and then decays to 1.2 V in about 40 ms, due to the diode’s thermal behaviour [16].

voltage over the selected magnet *B13L4* is queried from Post-Mortem and presented in figure 2.2. For the specific signal, first a short to ground occurs at a time of about 1.54 s, which causes an abrupt change of the magnet’s voltage from its previous value of about -11 V, which was obtained during the ramp up of the circuit current. In the circuit, a diode is connected in parallel to every magnet, which in case of a quench allows for the magnet to be bypassed as current flows through the diode instead. This behaviour can be seen in the measured signal around 1.6 s where the voltage peaks at a value of approximately 6 V, which is equal to the voltage drop of the diode. Attention should be drawn to the fact that the voltage will start decreasing after the peak value is reached, until a steady value of approximately 1.2 V is obtained, which is caused by the thermal effect of the diode, whose temperature increases as current flows through it. Although a quench follows the appearance of a short in this case, this is not a necessary condition, as one can happen at any time. In case such an event occurs, the circulation of the beam is immediately interrupted and the accelerator shuts down for a couple of hours. Despite this however, as long as a quench is detected in time and the protection systems are activated, it should not be considered dangerous, but rather a part of a magnet’s lifecycle.

2.3 Modeling the LHC Main Dipole Circuit

2.3.1 Modeling Background

The work presented in this thesis has been performed during a period of 10 weeks as part of the STEAM [17] collaboration of the TE-MPE-PE group [18] at CERN. Due to the complexity and the size of the LHC main dipole circuit, the modeling configurations regarding the main dipole magnets of the circuit have been drawn from previous work mentioned in [19] and [20]. The choices regarding the short to ground and fuse modeling

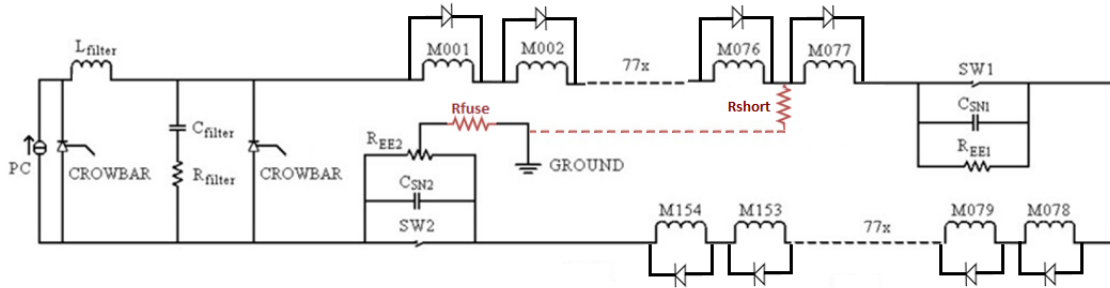


Figure 2.3: Electrical schematic of the LHC main dipole circuit [19]. Added in red: 1) a single short to ground between magnet $M077$ and ground 2) the fuse resistor in the grounding lines.

presented in the next sections, build on top of the netlist models of the main dipole circuit developed by *STEAM*. In terms of tools, the *STEAM PSpice Manager* tool package is used to solve the netlist models and parse the resulting simulated signals from the *PSpice* output *.csd* file to the *MATLAB* workspace for post-processing. The package also contains the *STEAM Stimulus Generator*, which allows the creation of stimuli starting from *CSV* files, that can be used as *PWL* inputs of various components in the netlist models.

2.3.2 Equivalent Model of the LHC Main Dipole Circuit and Magnets

Each of the 8 LHC main dipole circuits contain 154 superconducting magnets connected in series to the power converter. The equivalent model of the circuit, developed in *PSpice*, is presented in figure 2.3 and the modeling choices are thoroughly explained in [19].

In the schematic, the superconducting dipole magnets are represented by inductors connected in parallel to a bypass diode. However, in order to accurately model their nonlinear behaviour during transients, the more detailed model of figure 2.4 is introduced [19]. In the model, the subcircuits of the two apertures Ap_1 and Ap_2 are connected in series, with a resistor R_p and the bypass diode connected in parallel. The inductance of the apertures is represented by L , while the capacitors C model the coil to ground parasitic capacitance. The inclusion of the factor k in the inductance values as well as resistances R_1, R_2 achieve modeling of the induced eddy current effects. Table 2.2 provides a quick reference to the values of the above mentioned parameters, that have been calibrated in order to achieve the best match with the measured behaviour of the magnets [19].

When a short to ground occurs in the circuit, a low resistance path appears between the dipole magnet and ground. In figure 2.3, this is represented by resistor R_{short} . The main dipole circuit is connected to ground through the grounding system, where the fuse is also found. In its simplified form, the resistor R_{fuse} can be seen connected between the middle point of the energy extraction resistor R_{EE2} and ground. For both the short to ground and the fuse resistor only a brief introduction is given at this point, since these

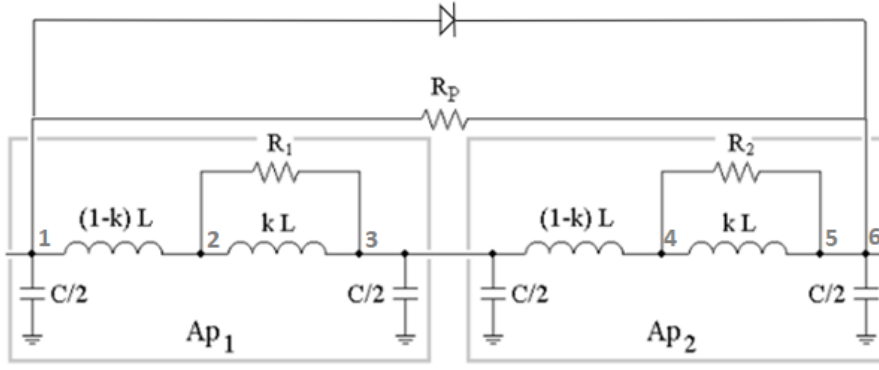


Figure 2.4: Circuit equivalent model of a LHC main dipole magnet [19].

Table 2.2: Parameters of Main Dipole Magnet Model.

Parameter	Value	Unit
L	49×10^{-3}	H
R_p	100	Ω
C	150×10^{-9}	F
k	0.75	-
R_1, R_2	$\in \{7, 10\}$	Ω

are the two additions to the model that will be discussed in detail in sections 3.1 and 3.2, respectively.

The whole sector is connected in series to the power converter, whose main function is to initially increase the circuit current with a certain ramp rate $\frac{dl}{dt}$ up to the specified nominal current value. The existence of the crowbar in parallel to the power converter allows the current to continue circulating in the circuit after the switch-off of the former, as is the case when a Fast Power Abort is triggered. The high frequency noise of the power converter is reduced by including a low-pass LC filter with a cutoff frequency of 31.8 Hz [19]. A second crowbar is connected in parallel to the filter, an addition that reduces the voltage waves propagating through the circuit following a power converter switch-off. After an initial period of current ramp-up, a steady state is reached for the voltage over the magnets, which is maintained under normal operation conditions.

2.3.3 Circuit Behaviour Following Fast Power Abort

In the case of extreme events occurring in the circuit, the non-linear behaviour of the various circuit elements leads to the appearance of transient effects that require thorough analysis and understanding. Common examples where these effects have been observed include Fast Power Aborts (FPA) as well as faults appearing in the circuit. During an FPA, most of the energy stored in the circuit is extracted, meaning that the current also decreases to a zero value. Although it is triggered in the case of unexpected events occurring in the circuit, including problems such as quenching magnets or related to the

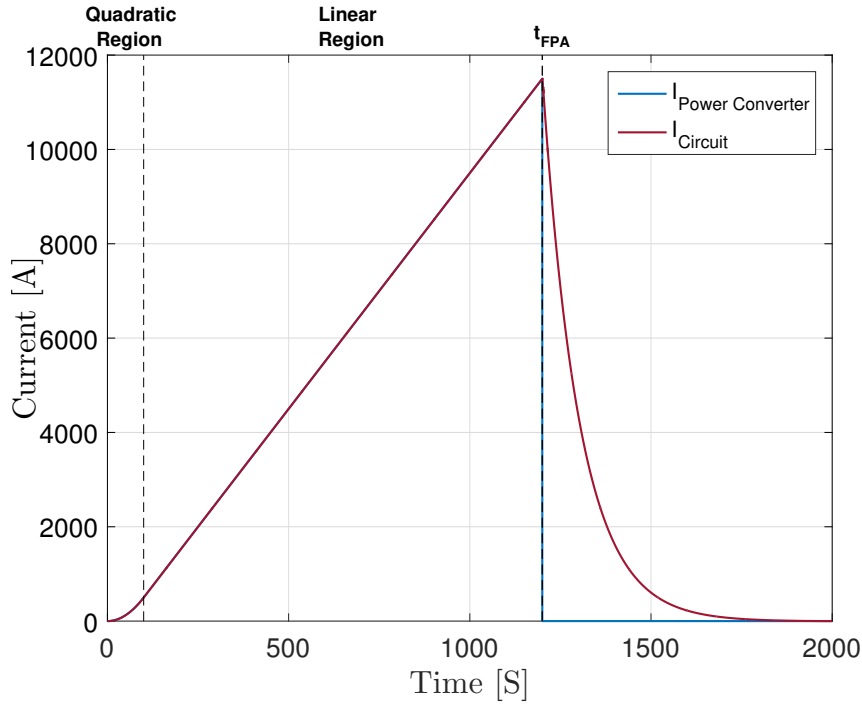


Figure 2.5: Plot of simulated power converter and circuit current. The abrupt switch-off of the power converter can be seen occurring at time t_{FPA} . The current in the circuit follows a semi-exponential decay to zero with a time constant of approximately 103 s.

power converter [19], power aborts have also been triggered in past years in order to carry out special tests [21]. These tests have resulted in the acquisition of measured signal data from various sensors in the circuit and for six different current levels, namely 760 A, 2 kA, 4 kA, 6 kA, 8 kA and 10 kA, which provide a better understanding of the circuit behaviour.

To gain a better idea of the current behaviour during the initial ramp-up, the plot of figure 2.5 is provided, where the increase of the current from zero up to its nominal value, at which point the FPA is triggered, is shown. In the figure, two regions can be identified, namely one where the current increases quadratically and one where it increases linearly. In the quadratic region the nominal ramp rate is equal to $\frac{d^2 I}{dt^2} = 0.05 \frac{A}{s^2}$, while in the linear region the current increases with a nominal rate of $\frac{dI}{dt} = 10 \frac{A}{s}$ [8]. It therefore becomes evident that the value of the current in the circuit at the time when the FPA occurs is a function of t_{FPA} as well as the nominal ramp rates of both regions.

Two energy extraction (EE) systems, namely EE1 and EE2 can be seen in the circuit. Each of them is composed of a switch in parallel to a resistor of approximately 73 m Ω . When the switches open, the energy extraction resistors become part of the circuit. This happens approximately 350 ms and 600 ms after the power supply switch-off [19] for the first and second switch respectively. The circuit current is hence forced to flow through the resistors and starts decreasing roughly exponentially, as shown in the plot of figure 2.5. The time constant of the decay can be calculated as shown in equation 2.1, where N_{mag} is the total number of magnets, L_{mag} the inductance of a single magnet and R_{EE} the value of the EE resistance [19].

$$\tau = \frac{N_{mag} L_{mag}}{2R_{EE}} \approx 103s \quad (2.1)$$

A first simulation can be performed in order to better understand the behaviour of the circuit in the case where no faults have occurred. In the simulations throughout this work, the current value when the FPA occurs $I(t_{FPA})$, is ramped-up to 11.5 kA. Although a slightly higher value was provided for the current at nominal field shown in table 2.1, the current loses its linear behaviour slightly before it reaches its peak value, making the value of 11.5 kA the last value where its ramp rate $\frac{dI}{dt}$ is still equal to $10 \frac{A}{s}$. With the chosen ramp rate, this current value is reached after 1200 s in the simulation. Choosing this current value will therefore provide consistency with the simulations investigating the worst cases that can occur in the circuit, that will be presented in following chapters.

Due to the large number of magnets, simulation results need to be plotted in such a way that useful conclusions can be drawn from the figures. For this reason, color coding using the jet colormap array [22] is used for the signals in the figures of this report, so that they can be easily read even with the legend omitted. The simulated voltages to ground plotted against two different axes, namely time and magnet electrical position, are presented in figure 2.6 for the case where a fast power abort is triggered and with no failures occurring in the circuit.

Starting with figure 2.6a, the voltages to ground are plotted against time. In this plot, the time when the power converter switches-off t_{FPA} as well as the moments when the EE switches open t_{EE1} and t_{EE2} become easily distinguishable, since a time window including all three of them is chosen. As can be seen in the figure, these events occur at times 1200 s, 1200.36 s and 1200.57 s, respectively. They are the main reason for the appearance of transients in the circuit, which can be observed right after the specified times and are followed by changes in the voltage to ground values and polarities of the magnets. After time t_{EE2} , when both EE resistors are in series with the magnets, the current in the circuit starts its semi-exponential decay until it reaches a zero value, with the voltages to ground of all magnets also showing this decay.

In the plot of figure 2.6b, the voltage to ground values at specific times are plotted against the electrical position of the magnets in the chain. This allows to better observe the voltage distribution in the circuit and how it varies over time. The first time chosen is at 1200 s, for which the voltage distribution exactly at the time when the FPA occurs is plotted. The initial voltage to ground at magnet 1 in this case has a value of about 150 V, calculated as a function of the total circuit inductance $N_{mag} L_{mag}$ and the initial ramp rate of the current $\frac{dI}{dt}$. The resistance of the warm copper cables R_{warm} , which precede the first magnet of the chain, also need to be taken into consideration and hence the expression used to calculate the voltage value of the first magnet, is presented in equation 2.2. The fact that all magnets have the same inductance value causes the total circuit voltage to be linearly distributed across the chain. A linear voltage decrease of about 1 V is observed when moving from one magnet to the next until an almost zero value is reached for the last magnet of the chain, which is connected to the grounding point of the circuit.

$$V_{PC} = R_{WARM}I + N_{mag}L_{mag}\frac{dI}{dt} \quad (2.2)$$

The following two time points, namely 1200.40 s and 1200.78 s, are chosen after the transient effects that follow each EE switch opening have died-off, as can be seen in figure 2.6a. At the time of 1200.40 s, the first energy extraction resistor has become part of the main circuit loop. For a current value of 11.5 kA when the FPA occurs in the simulation and an energy extraction resistance of about 73 mΩ, the voltage drop that occurs over the resistor is approximately equal to 800 V. Since the first energy extraction system is connected in between magnet 77 and 78, this voltage drop can be observed in the figure when looking at the middle of the magnet chain.

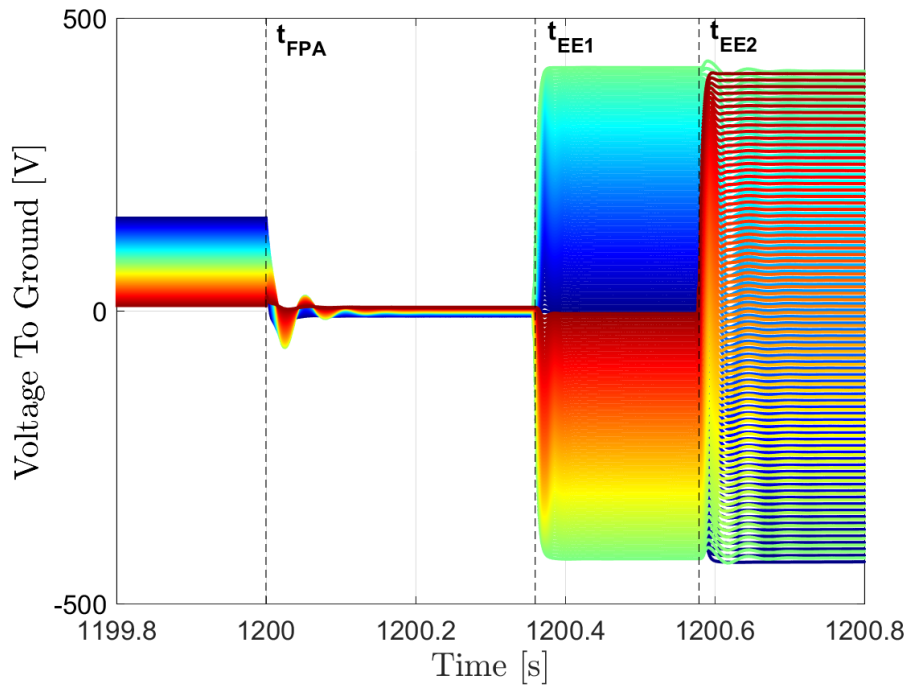
The voltage is again equally distributed over the circuit magnets and a voltage difference of approximately 5 V is observed between the values of neighbouring magnets. The maximum values for the case where a single energy extraction resistor exists in the circuit, can be seen obtained by the magnets in electrical positions 77 and 78 and are equal to a value of $\pm \frac{R_{EE}I}{2}$. Values close to 0, which are minimum when absolute voltage values are considered, are obtained by both magnet 1 and 154 for this case.

For the final time of 1200.78 s chosen in figure 2.6b, both energy extraction switches have opened and voltage drops occur over both EE resistors. An expression for the value of the voltage drop over the two resistors as a function of $I(t_{FPA})$ and the total EE resistance, is provided in equation 2.3 [19].

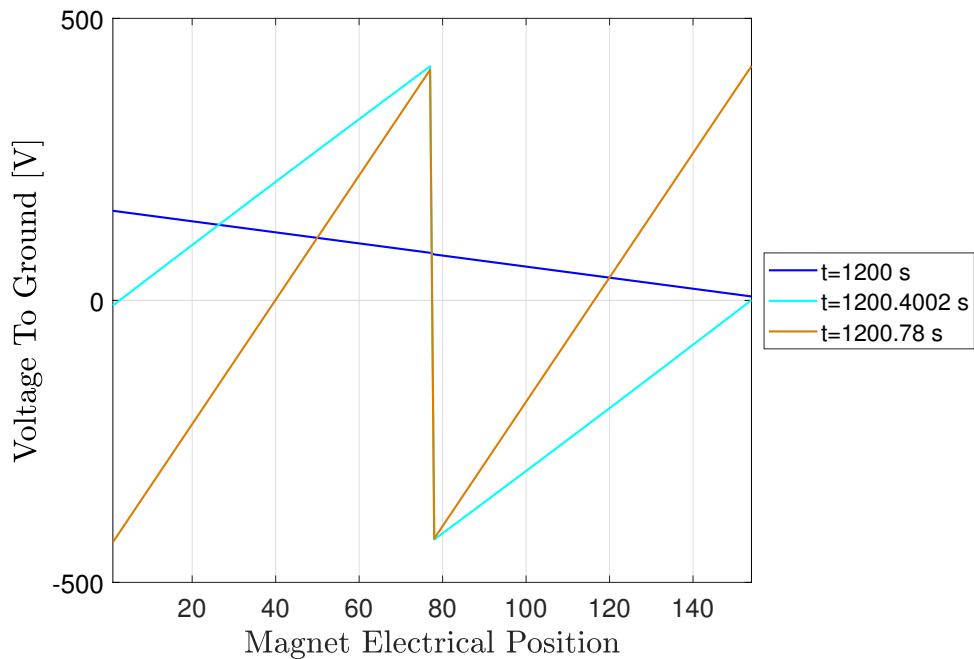
$$V_{magnetChain} = -2R_{EE} \cdot I(t_{FPA}) \quad (2.3)$$

When both switches have been opened, the voltage difference when moving from one magnet to the next at the regions where a linear increase is observed, is equal to approximately 11 V and can be calculated by dividing equation 2.3 by the total number of magnets. The same maximum voltage to ground value equal to $\pm \frac{R_{EE}I}{2}$ is also observed in this case, with the difference that it is obtained by four magnets instead of only two previously and more specifically the ones at electrical positions 1, 154, 77, 78. The magnets in the middle of each half chain, namely 39 and 116, obtain voltage to ground values approximately equal to zero, since the voltage is once again distributed evenly over all magnets in the chain.

Following the above analysis, a first identification of the peak voltage to ground values obtained in the LHC main dipole circuit has been achieved. For the case when a FPA occurs without any fault appearing in the circuit, the peak voltage value is approximately equal to 0.4 kV and is obtained by the magnets before and after the first energy extraction resistor as well as the first and last magnet of the circuit.



(a) Simulated voltage to ground signals for all 154 magnets plotted as a function of time. The times when the FPA occurs and the EE switches open are also visible. All three events are followed by transients and occur within less than 1s after the FPA. The signals are color-coded as a function of the magnet position in the chain starting with blue for the magnet in electrical position 1 and scaling up to red for the magnet in position 154.



(b) Simulated voltages to ground plotted for specific time instances as a function of the electrical position of the magnets in the main dipole chain.

Figure 2.6: Two graphical representations of simulated voltage to ground signals for all 154 magnets in the chain.

CHAPTER 3

WORST-CASE ANALYSIS OF SHORT-CIRCUIT TRANSIENTS

3.1 Modeling Short Circuit to Ground

Different types of short circuits to ground can occur in an accelerator circuit. The LHC main dipole circuit consists of various electrical components and magnets, which implies that faults can appear in any part of the chain. This work will concentrate on single shorts to ground occurring between a magnet in the LHC main dipole circuit and ground during operation. Starting from the existing netlist circuit model, a method to include the short connection that can unexpectedly appear between a superconducting magnet and ground is first described.

The method chosen to achieve this is by the inclusion of a voltage controlled switch in the model between the point where the short occurs and ground. More specifically with the closing of the switch, a connection between two nodes (node where the short occurs and ground) is created, which can easily change back to an open circuit when the switch opens. Due to the fact that the existence of a short circuit is from an electrical perspective equivalent to a finite value resistor establishing the connection, its resemblance to the behaviour of the voltage controlled switch becomes visible and its addition to the netlist model can hence be justified.

The netlist implementation of the component is shown in figure 3.1, with the short occurring at magnet 77. The subcircuit consists of a voltage source connected to a node independent of the rest of the circuit, in this case called *control*, with the voltage of the source obtaining either the value of 1 or 0. In terms of the nodes that were used in figure 2.4, the connection to ground occurs between node 1 and the ground of the magnet, which is specified in the first line of figure 3.1. As the names of the parameters suggest, when the switch is open, it acts as an open circuit due to the resistor R_{off} been set to $1\text{ M}\Omega$, while when the switch is closed, resistor R_{on} sets the short to ground

```

*Short-to-ground model
xShort ( MAG77 MAG_Gnd77 ) ShortCircuit
+ PARAMS: R_short=1

.subckt ShortCircuit 1 2
+ PARAMS:
+ R_short=1
S1 (1 2 control 0) SwitchShort
v_S1 (control 0) STIMULUS = ShortSwitchVoltage
.model SwitchShort VSWITCH Voff=0.0 Von=1.0 Roff=1e6 Ron={R_short}
.ends

```

Figure 3.1: Netlist implementation of short circuit between one side of magnet 77 and ground as a voltage controlled switch.

resistance equal to the variable R_{SHORT} . Another important detail to notice is the use of a stimulus for the voltage of the controlling voltage source, which specifies the time its voltage switches from 0 to 1. For the simulation, in the stimulus it is essential to specify the last time index when the voltage has a value of 0 as a couple ms before the time when the switch occurs. This forces the solver to execute the switching during the in-between time, avoiding hence a potential slow ramp up of the voltage that would cause the model to diverge from the circuit's physical behaviour.

With the position and the resistance of the short to ground being the independent variables, it follows that the analysis of simulation results for different position and resistance values can provide a better understanding of the circuit behaviour. Although a finite number of possibilities, equal to the number of magnets in the circuit, exist for the position where the short can appear, its resistance can take any value in the set of real numbers. However, resistances above and below a certain value act either as an open or a short circuit, respectively and a change past those ranges has no significant effect. Hence, by choosing 5 resistance values from the in-between set, the effect of the resistance can be understood for certain ranges instead of discrete values. The chosen resistance values are $[0.001, 1, 10, 100, 1000] \Omega$.

For values larger than 1000Ω , the current flowing through the short obtains a small value and hence those values can be considered an open circuit. For the main dipole circuit, it is important to mention that the short resistance is in series with the equivalent resistance of the earthing system, which is in the order of 10Ω . Hence, it is expected that resistance values lower than 1Ω have little impact to the total equivalent resistance of the ground.

Making use of the Low-Level File I/O package in *MATLAB*, the value of the short position and resistance can be read and changed programmatically in the main netlist file or one of its subcircuits. This allows for an automated workflow to be developed, enabling a parametric sweep to be performed for the above mentioned input parameters. As a result, a large amount of data containing the simulation results for 154 different short positions and 5 different short resistance values, can be saved recursively in an organised way. A link to the code scripts implementing the above can be found in the repository provided in Appendix A.4.

3.1.1 Circuit Behaviour Following Single Short Circuit to Ground

As an example, a simulation can be performed for a short between magnet 70 and ground, which appears at time $t = 1202$ s. Due to the fast decay of the current in the circuit and the need to investigate the conditions leading to worst cases, the time at which the short occurs is chosen closely after the transient oscillations, caused by the opening of the EE2 switch, have died off. This ensures that the value of the current in the circuit has not decreased majorly from its peak value. The behaviour of the current around the time when the FPA is triggered can be seen in figure 3.2. The exact value of the current at $t = 1202$ s, when the short occurs, can also be specified as being almost equal to 11.3 kA, meaning that the current has decayed by 2 % of its maximum value. The results of this simulation for the voltages to ground of all the magnets in the circuit are plotted in figure 3.3a and 3.3b as a function of time and electrical magnet position, respectively.

With no change made to the simulation parameters, no variation is expected in the curves of figure 3.3b before the time when the short occurs, which are plotted as dashed lines and match the ones presented in figure 2.6b. For all times after $t = 1202$ s, when the short occurred, a shift of the curve along the y axis, corresponding to a change in the voltage to ground distribution along the circuit can be observed in the curve, which brings the voltage to ground of the magnet where the short occurred close to zero. With a negligible short resistance value, the voltage to ground of the shorted magnet becomes equal to zero, since a direct connection to ground is present. However, although it is true that the voltage to ground at the shorted magnet greatly decreases and obtains

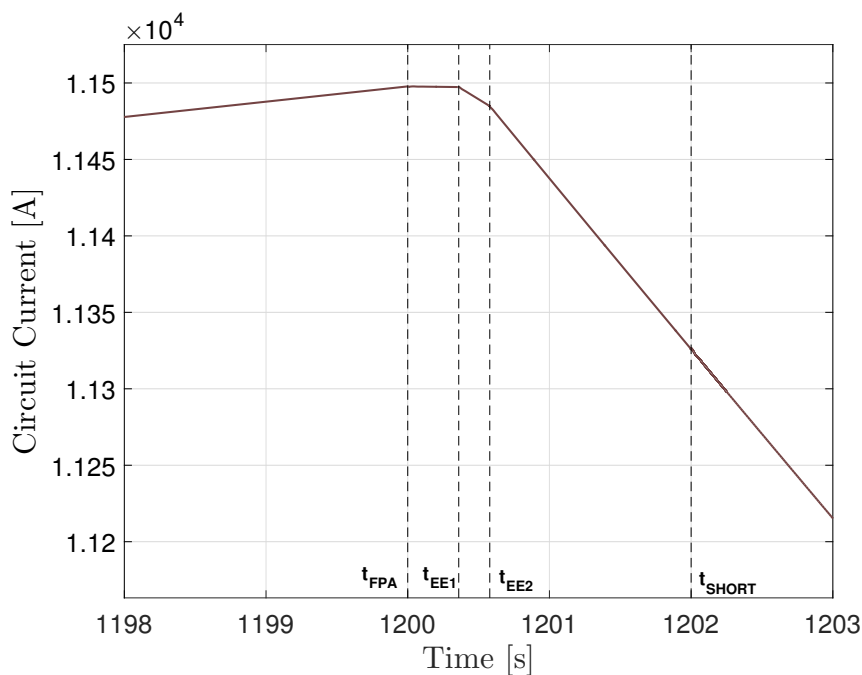
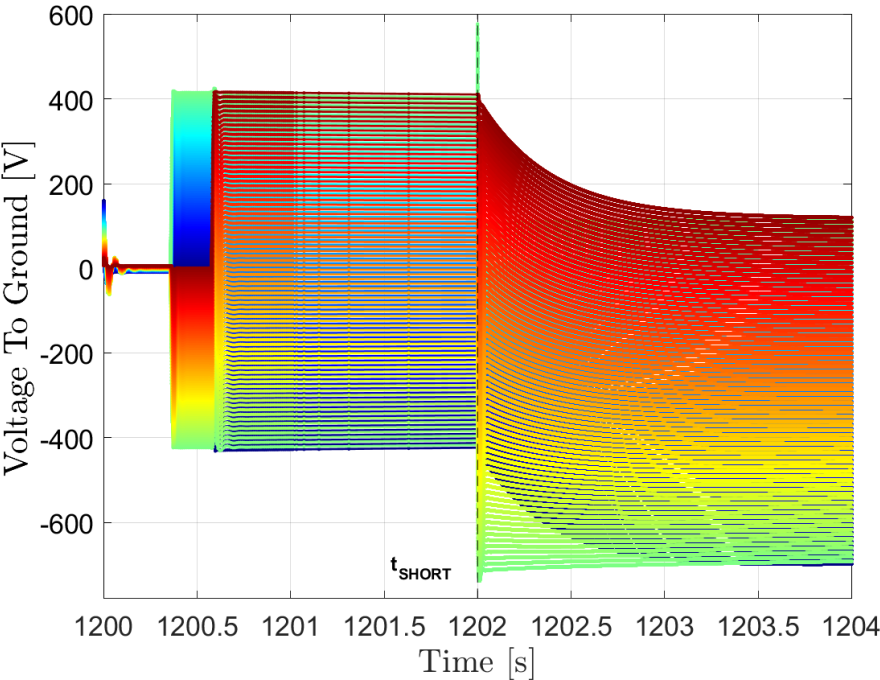
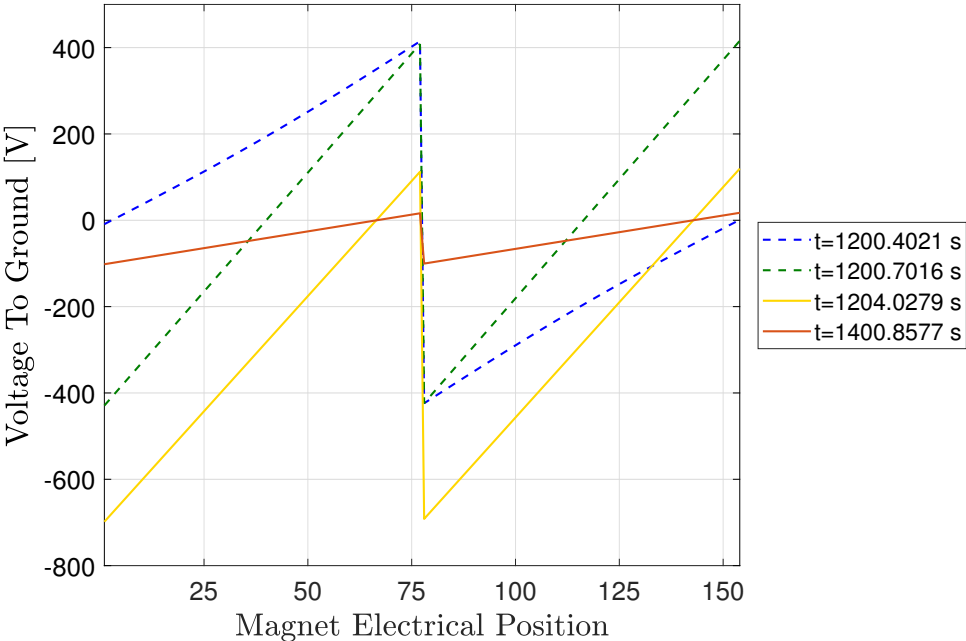


Figure 3.2: Detail of circuit current in circuit for the time window including t_{FPA} and the beginning of the decay.



(a) Simulated voltage to ground signals for all 154 magnets plotted as a function of time, with the FPA, EE1 and EE2 times specified. A short occurs between magnet 70 and ground at $t_{SHORT} = 1202$ s with a short resistance of $R = 1 \Omega$.



(b) Simulated voltage to ground values of subfigure 3.3a plotted at specific time points before (dashed line) and after the short, as a function of the electrical magnet position.

Figure 3.3: Two graphical representations of all 154 magnet voltage to ground signals for the case with a short appearing between the magnet in electrical position 70 and ground at 1202 s with a resistance of $R = 1 \Omega$.

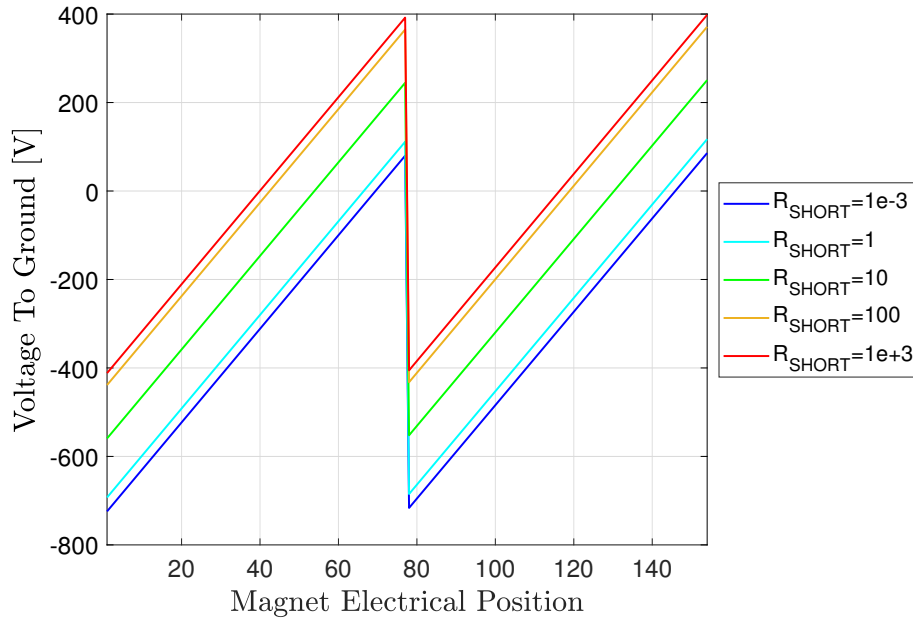


Figure 3.4: Simulated voltages to ground for all magnets at time $t = 1208$ s with a short occurring at magnet 70 at $t = 1202$ s. For the curves, short position and time the short occurs remain constant, while the value of the short resistance is varied.

a minimum value when compared to the rest of the magnets, an exact zero value is never obtained due to the voltage drop being a function of the short resistance value, $V_{SHORT} = R_{SHORT} I_{SHORT}$. Finally, the exponential decay of the voltages to zero can be visualised once again by plotting the voltage distribution of the magnet chain at a chosen time of about 200 s after the short occurred, where all the magnet voltages have been reduced, following the total circuit current behaviour of figure 2.5.

From the above, the effect of varying the short resistance also becomes clear, which visually corresponds to a shift of the curve along the y axis, as seen in figure 3.4. For a short occurring at a specific magnet, the change of the short resistance relative to a previous value, determines the change of the voltage to ground value at the specific magnet and consequently all of the other magnets in the chain. The effect of variations in the values of the two other independent variables, namely short position and time the short occurs, are presented in figures 3.5 and 3.6 and are discussed next.

The effect of the time when the short occurs is closely connected to the behaviour of the current in the circuit presented in figure 2.5 and its exponential decay. In figure 3.5, with the short occurring between magnet in electrical position 70 and ground with a resistance of 1Ω , a change in the slope of the curves is caused by a variation of the time at which the short occurs. More specifically, the 3 different times that are chosen for the short to appear are 1202 s, 1247 s and 1300 s, with the voltage at the electrical magnet position plotted for approximately 1 s before (dotted line) and approximately 2 s after each chosen time point. As expected, for the time instances before the short, the minimum voltage to ground is achieved in the middle of each half chain, with the position shifting to magnet 70 for the times following the short appearance. For all times after the short, the voltage closest to zero remains the one of the shorted magnet, with

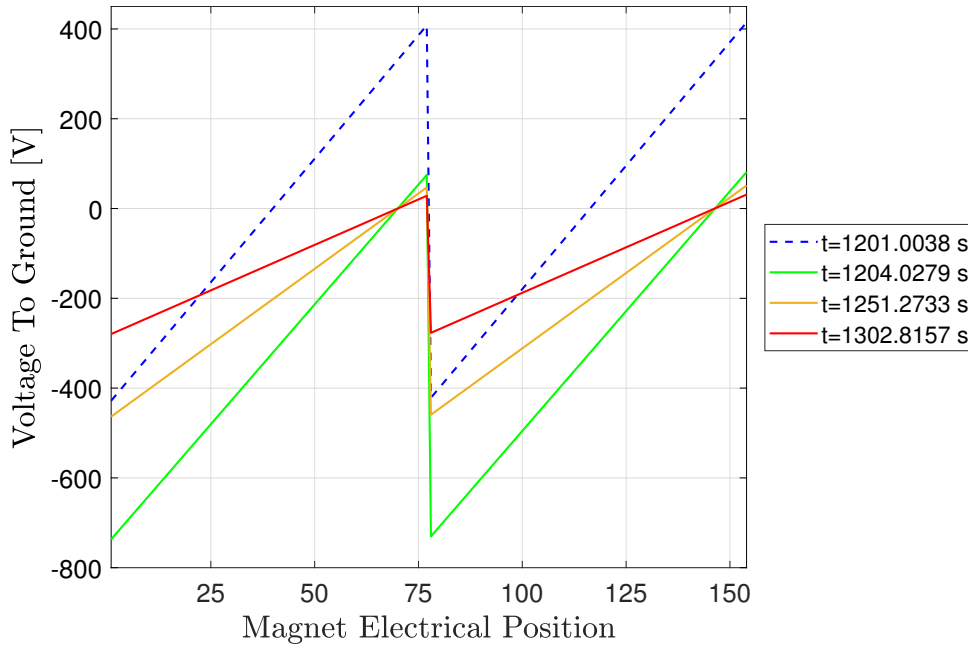


Figure 3.5: Simulated voltage to ground signal values at different time instances with a short occurring at magnet 70 at $t=1202$ s. For the curves, the short occurred at magnet 70 with a short resistance of $1\ \Omega$. The position and resistance value of the short remain constant so that the effect of varying the time the short appears can become visible.

the difference being a decrease of the total voltage drop that is equally distributed over the magnets for later times due to the decay of the circuit current.

The shifting of the curve due to the voltage drop obtaining a minimum value at the magnet where the short occurs can also be used to define the worst cases that can appear in the circuit for the case where a single short has occurred. It can hence be said that when the short appears between magnets in positions 1, 77, 78 or 154 and ground, the peak voltage to ground value is obtained in the circuit. Each of these magnets is connected on either side of the two EE resistors of the circuit, where the highest voltage drops occur. When a short occurs at one of these magnets, the total voltage distributed over the half chain adds up to the magnet at the opposite end, which obtains the peak value. The equation to calculate the peak voltage to ground value as a function of the current at the moment the FPA occurs I_{FPA} and the value of the total EE resistance R_{EE} , is presented in equation 3.1.

$$V_{MAX} = I_{FPA}R_{EE} \quad (3.1)$$

It is important to note that with a short occurring at the specified magnet positions, this value is twice higher than the peak voltage to ground in absence of shorts to ground derived in subsection 2.3.3. In figure 3.6, the voltage distribution curves for the 4 previously mentioned short positions that obtain the maximum voltage values are plotted. Evaluating the equation for the maximum current value of $11.85\ \text{kA}$ in the LHC main dipole circuit and the value of each EE resistor equal to $73.3\ \text{m}\Omega$, it follows that the maximum voltage value that can be achieved is equal to approximately $870\ \text{V}$.

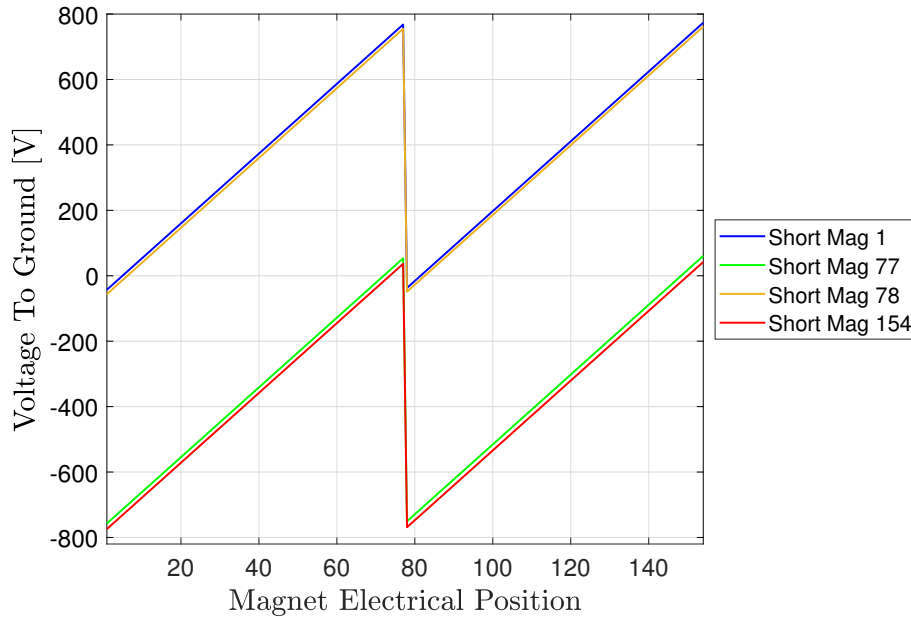


Figure 3.6: Simulated voltage to ground values for all magnets at the time of $t = 1208$ s with a short occurring between 4 different magnet positions and ground at $t = 1202$ s. The short position is varied in this case while the time the short appears and its resistance remain constant.

3.2 Modeling Circuit Fuse Blow-Up Behaviour

The series of magnets in each LHC main dipole circuit, is grounded to earth through the grounding lines connected to the middle point of the EE2 resistor. In its simplest form, the inclusion of the fuse in the model of the main dipole circuit has been shown in figure 2.3, since a resistor connected to the subcircuit model of R_{EE2} is effectively in series to the path of the circuit current to ground. In a more precise model, the energy extraction resistor consists of 4 resistors placed in a parallel branch configuration, where resistors R_{EE2_1} and R_{EE2_2} are in series and the fuse is connected between R_{EE2_3} and R_{EE2_4} . Taking into account all the electrical components that compose the grounding subcircuit as well as its exact connection point with the resistor R_{EE2} , a more accurate schematic is provided in figure 3.7.

Placing a fuse in series with a specific branch of an electrical circuit ensures its protection from the circulation of currents with values above a certain threshold when the fuse is blown up. It follows hence, that depending on the state of the fuse, the grounding subcircuit of figure 3.7 obtains different resistance values. For the specific circuit, the fuse has a resistance of 1Ω , while it can be considered that it obtains an infinite value after a specified threshold is reached, at which it blows up. In this case, the current can only flow through the $10 \text{ k}\Omega$ resistor to ground connected in parallel.

For the case where the fuse has not blown up, the total resistance of the grounding subcircuit is calculated from the parallel connection of the two branches having resistance values of 11Ω and $10 \text{ k}\Omega$ respectively, which results in a total resistance of 10.99Ω . In figure 3.7, two back to back diodes can also be seen connected in parallel to the 10Ω

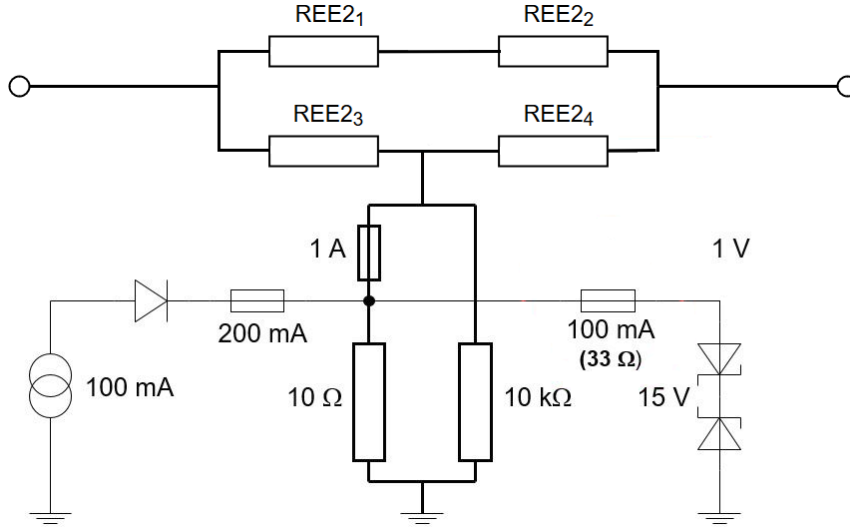


Figure 3.7: Grounding subcircuit including fuse, which achieves connection of the LHC main dipole circuit to earth.

resistor, which start conducting after the voltage exceeds the value of 15 V. When this happens, a resistor of 33 Ω is also connected in parallel to the 10 Ω resistor, which makes the resistance of the left branch equal to 8.67 Ω and hence the total subcircuit resistance obtains a value of 8.66 Ω .

With the configuration shown in the figure, it also becomes clear that the fuse subcircuit can be considered effectively in series to the short to ground analyzed in the previous section. After the blow-up of the fuse, a high resistance value is obtained by the grounding subcircuit and hence the current flowing through the short is also limited. The final expression for the equivalent resistance to ground, depending on the state of the fuse, is presented in 3.2.

$$R_{eq} = \begin{cases} R_{SHORT} + 10.99 \Omega, & \text{if fuse not blown up \& } V_{DiodesGND} < 15 \text{ V} \\ R_{SHORT} + 8.66 \Omega, & \text{if fuse not blown up \& } V_{DiodesGND} \geq 15 \text{ V} \\ R_{SHORT} + 10 \text{ k}\Omega, & \text{if fuse blown up} \end{cases} \quad (3.2)$$

In the datasheet of the fuse, the threshold values regarding its blow-up behaviour are specified and together with its resistance value are presented in table 3.1.

Table 3.1: Parameters of Fuse.

Parameter	Value	Unit
R_{FUSE} (If not blown up)	1	Ω
Pre-arcing Threshold	0.23	A^2s
Blow up Threshold	1.2	A^2s

A further elaboration is needed for the threshold values and their units, since two

different ones are provided. More precisely, the two values refer to the thermal thresholds of the fuse, meaning that a direct relation to the energy deposited in the fuse is drawn. The value of the thermal load can be calculated as the time integral of the square of the fuse current over time $\int I_{FUSE}^2 dt$, measured in A^2s , with an initial value at time t_{SHORT} , when the short occurs, equal to 0. With the specified values, the fuse blows up shortly after time t_{SHORT} , when current starts flowing through it.

From experimental data, it has been observed that in the pre-arcing region, the fuse enters a state of uncertainty, where it intermittently blows up and recovers. After the blow up thermal limit is reached however, it can be said that the fuse acts as an open circuit, since it has blown up.

It becomes clear that in order to model the fuse blow up behaviour, the current flowing through it needs to be known so that the state of the fuse can be altered once the thermal thresholds are reached. There is currently however no component in the Spice language that can monitor the current in real time and force the fuse to change its state when a certain condition is met. For simulations included in past case studies, the time of the blow up was set up manually for each simulation. Therefore, in order to create a model that accurately represents the blow up behaviour of the fuse, a new method has to be developed.

Following the same logic as with the modeling of the single short to ground, the fuse resistor is replaced by a voltage controlled switch in the model. The circuit parameters as well as those of the short to ground (position, resistance value) are required as user input for the simulation to begin. With these values, a first *PSpice* simulation for the case where the fuse never blows up is performed, from which only the signal of I_{FUSE} is returned in the *MATLAB* workspace, so that the required computational power and time are reduced. Applying the trapezoidal rule on the signal data, the numerical integral of the square of the dataset is computed, hence obtaining the thermal load of the fuse. The point in time when the value of the blow-up threshold is reached can then be found.

With the time when the lower threshold is reached known, pulses can be triggered starting from that point until the end of the simulation, occurring with a specific frequency. For the specified frequency value, the calculation of on and off times is performed by *MATLAB*, which also inserts them in the stimulus file of the fuse. A simulation is then run in *PSpice* with I_{FUSE} returned to the *MATLAB* workspace after its end. The signal of the current through the fuse under the effect of switching pulses has now been captured and is numerically integrated in *MATLAB* to obtain the time the second threshold is reached. After the blow-up limit of the fuse is found, the stimulus is again overwritten, with pulses starting at the pre-arcing threshold and ending when the second threshold is reached, after which the switch stays open. The final simulation is then run, with the data saved in a nested structure array, indexed with the magnet position number where the fault occurred. When compared to a simulation scheme that does not include the blow-up behaviour of the fuse, the specific method increases the accuracy of the model. On the other hand, the additional simulations than need to be performed in order to obtain the current profile of the fuse, increase the overall simulation time. A flowchart summarising the steps followed in the proposed simulation scheme is shown in figure 3.8.

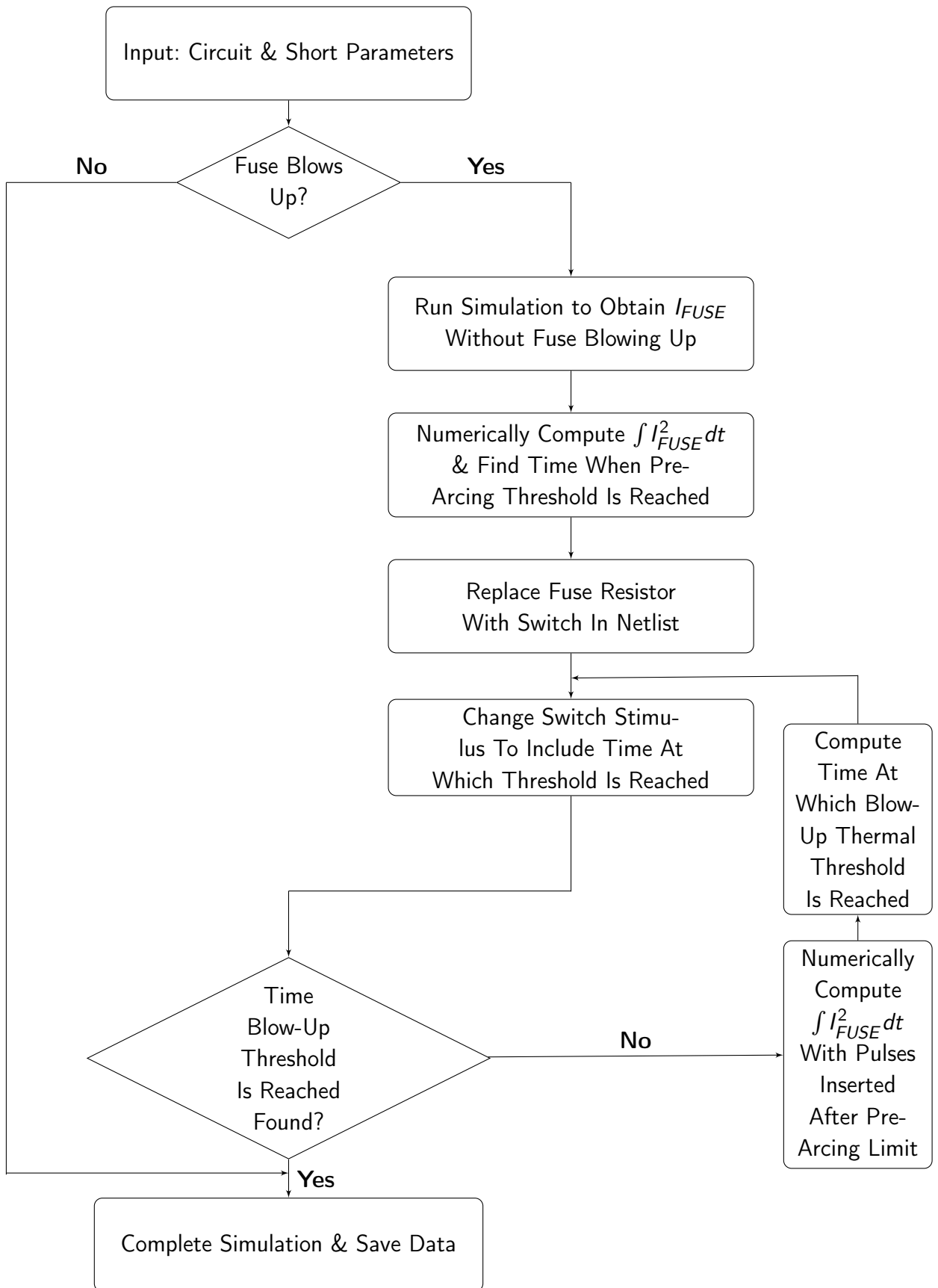


Figure 3.8: Block diagram of simulation scheme proposed in order to include the blow-up behaviour of the fuse in the model.

3.3 Circuit Behaviour Following Fuse Blow-Up and Identification of Worst-Cases

The behaviour of the fuse current I_{FUSE} over time for the simulation scheme including the fuse behaviour is presented in figure 3.9. The current through the fuse in the case where no blow up occurs in the simulation is also included for reference in the same figure. For the case where the fuse does not blow up, the current through it will continue to increase as shown in the figure, eventually reaching a peak value of about 32 A, after which it decreases almost exponentially to zero. On the other hand, the pulses that are triggered after the pre-arcing threshold is reached, become clearly visible in the case where the fuse behaviour is included in the simulation and last for about 30 ms. It is interesting to note that the maximum amplitude of the current during the intermittent blow-up behaviour of the fuse is less than the peak current value obtained in the case of no blow-up, which is reached right before the current starts decaying to zero.

Proceeding with the voltage to ground plots for the case where the fuse blow up behaviour is modeled, the same two plot configuration for the visualisation of the voltages to ground at all magnet positions that has been presented previously in figures 2.6 and 3.3 for the cases when no short occurred and the fuse did not blow up is used, with the plots presented in figure 3.10. For the simulations, the same parameter choices as in previous parts of the thesis have been made, with the short occurring between magnet 77 and ground at time $t=1202$ s and with a short resistance of $1\ \Omega$.

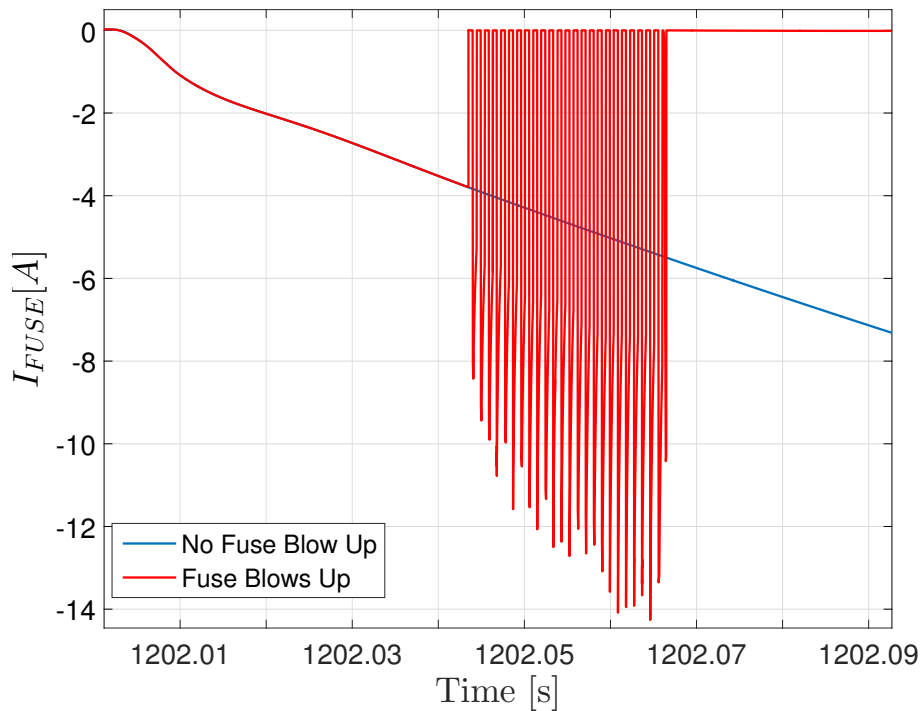
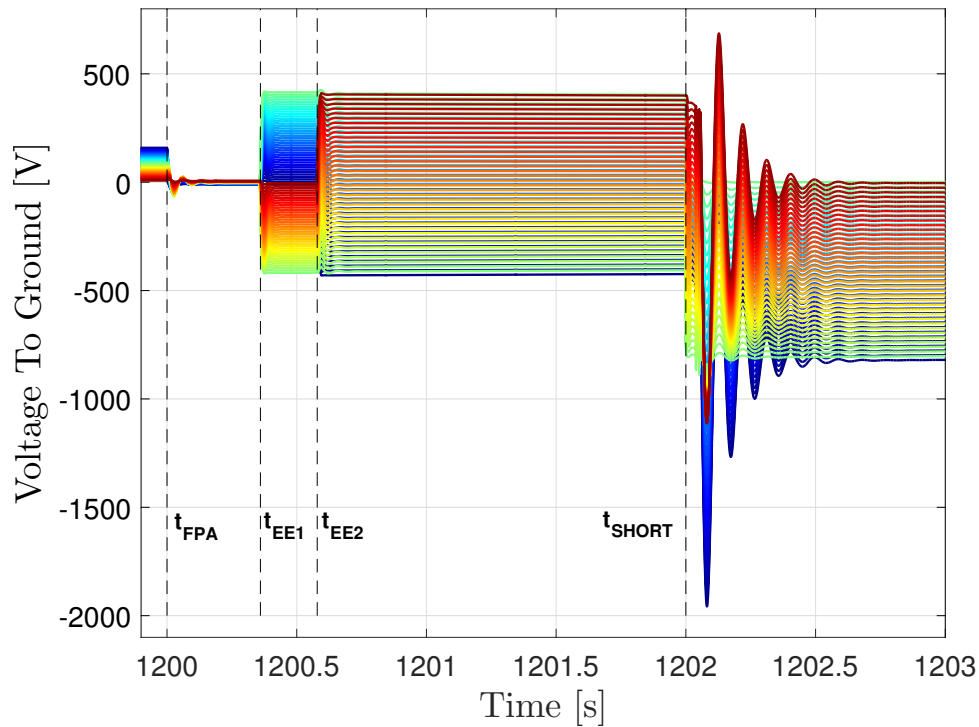
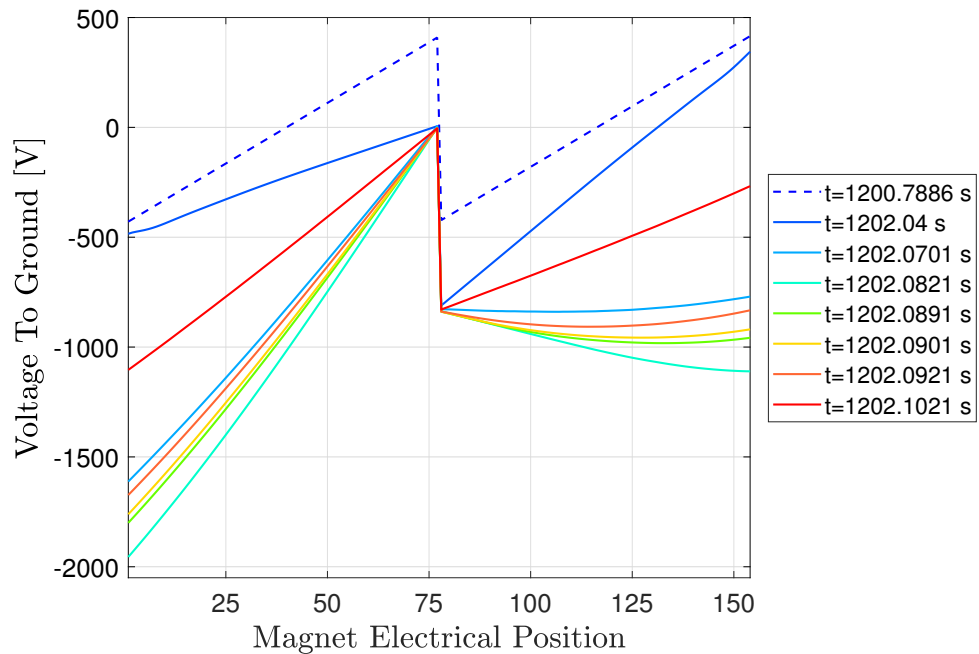


Figure 3.9: Comparison of simulated I_{FUSE} signal over time obtained from a simulation including the fuse behaviour and one where the fuse did not blow up. The short to ground in both cases occurs at magnet 77 and has a resistance value of $R_{SHORT}=1\ \Omega$.



(a) Simulated voltage to ground signals for all 154 magnets plotted as a function of time, with the FPA, EE1 and EE2 times also specified. A short occurs at magnet 77 at $t_{SHORT} = 1202$ s and with a short resistance of $R = 1 \Omega$, while the fuse blow-up behaviour is included in the simulation.



(b) Simulated voltages to ground of subfigure 3.10a plotted for specific times before (dotted line) and after the short, as a function of the magnet's electrical position.

Figure 3.10: Two graphical representations of all 154 magnet voltages to ground for the case of a short appearing between magnet 77 and ground at 1202 s with a resistance of $R = 1 \Omega$. The blow-up behaviour of the fuse is included in the simulations.

3.3. CIRCUIT BEHAVIOUR FOLLOWING FUSE BLOW-UP AND IDENTIFICATION OF WORST-CASES

In the figure, it can be seen that the peak voltage to ground after the fuse blows up reaches an absolute magnitude of about 2000 V. As expected from the analysis presented in subsection 3.1.1, when a short appears at magnet 77, the peak value is achieved by the voltage to ground signal of magnet at electrical position 1. This value is obtained approximately 140 ms after the blow up threshold is reached. After the voltage to ground signal reaches its peak value, a slow decrease to a value of about 1950 V occurs in about 10 ms, after which the voltage starts rapidly decreasing. Drawing a comparison with figure 3.3a, the peak voltage value in this case is higher than the one obtained in the case where the fuse behaviour was not simulated and which was analytically calculated using equation 3.1.

In order to better understand the increase of the peak voltage to ground, it is helpful to look at figure 3.10b. An obvious difference is observed between the voltage distributions at times higher than 1202.07 s when compared to the ones before that time, with a change in the polarity of the voltages to ground and hence the slope of the curves observed for the magnets in positions higher than position 77. The voltage drop across each magnet corresponds to the opening voltage of about 6 V of the by-pass diode, which is connected in parallel to each dipole magnet. In figure 3.11, it can be seen that the bypass diodes in parallel to the magnets of the second half of the chain are conducting during the same time window.

For the time instance of 1202.0821 s, the voltage to ground at magnet 154 reaches a value of about 1060 V. The voltage drop over the second EE resistor, which is connected in series following magnet 154 and preceding magnet 1, has a value of about 900 V at the chosen time. This results in a value of about 2000 V been reached by the voltage to

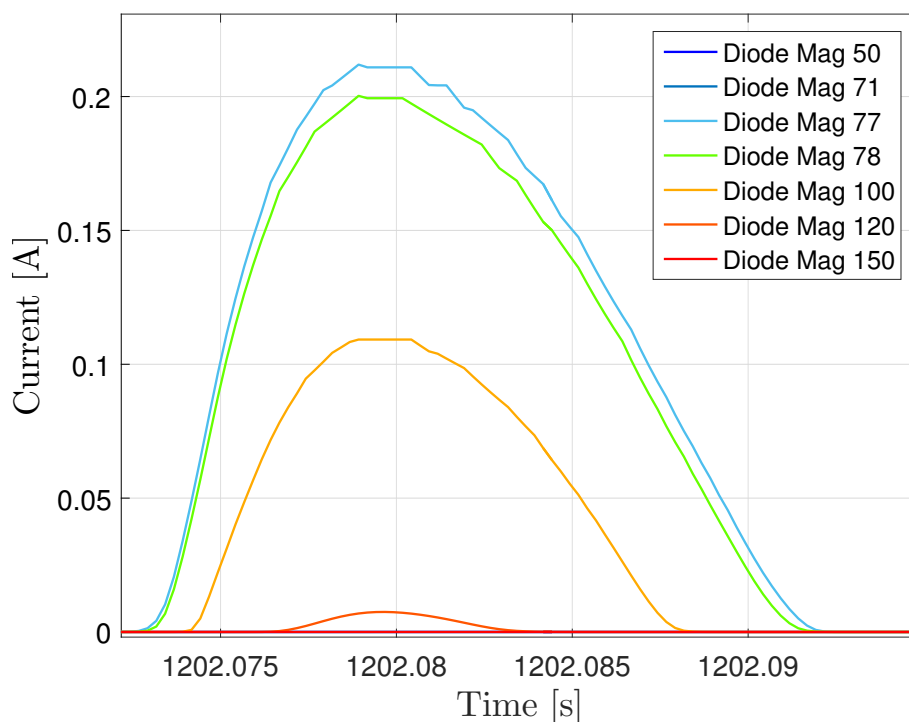


Figure 3.11: Current over time through bypass diodes of selected magnets both in electrical positions before and after the magnet where the short to ground occurred.

ground of magnet 1.

From this analysis, it becomes clear that a new formula for the analytical calculation of the peak voltage to ground needs to be provided. This can be achieved with the expression provided in equation 3.3, where N_{mag} is the total number of magnets in the circuit, R_{EE} the EE resistance and V_D the diode voltage drop.

$$V_{MAX} = 2I_{FPA}R_{EE} + \frac{N_{MAG}}{2} V_D \quad (3.3)$$

Considering the current at nominal field for the LHC main dipole circuit, which is equal to $I = 11.85\text{ kA}$ and each EE resistor as having a value of about $73\text{ m}\Omega$, the maximum value for the voltage to ground that can be achieved in the circuit is equal to about 2.2 kV .

It is important to verify that the value is independent of the frequency of the pulses inserted between the two fuse thermal thresholds. Due to the fact that uncertainty characterises the region following the pre-arcing threshold, the choice of the frequency with which the pulses are triggered in the simulation is arbitrary and should not alter the results of the worst case. Since a voltage to ground close to the maximum possible value has been obtained by magnet 1 for the case where the short occurs between magnet 77 and ground, the same simulation can be performed with frequency values at different orders of magnitude.

In figure 3.12 it can be seen that when pulses are triggered with lower frequencies, higher current values are reached than the ones when pulses are triggered with higher frequencies. However, in terms of voltage, as shown in figure 3.13, the value of the frequency has the opposite effect on the peak voltage to ground, with higher values of frequency causing higher peak amplitudes, which are all similar in value. From the figure it also becomes interesting to note that every time a pulse occurs, the slope with which the voltage starts decreasing remains the same, which means that the value of $\frac{dI}{dt}$ also stays the same. Hence, the similarity between the pulses for a single frequency can be seen, which also makes clear that was it not for the pulse switch off, the voltage would have the same oscillatory behaviour as seen after the fuse reaches the blow-up threshold. As a conclusion of this analysis, it follows that although the frequency set for the pulses in the simulation has an effect on the peak value of the voltage drop, it is not a parameter that alters the worst case found for the peak voltage to ground in the circuit.

Up to now the analysis has been concentrated on the simulation results obtained for a short that occurred between magnet 77 and ground and a short resistance of $1\ \Omega$, two parameters that are set in the beginning of the simulation. A parametric sweep of these parameters can easily be performed by programmatically changing their values and simulation results are obtained for all short positions in the range of [1:154] and for 5 different short resistance values with different orders of magnitude, namely [0.001, 1, 10, 100, 1000] Ω . The results of the analysis are summarised in the color plots of figures 3.14 and 3.15 where the colors contain information about the peak voltage to ground values obtained for different short positions, magnet electrical positions as well as short

3.3. CIRCUIT BEHAVIOUR FOLLOWING FUSE BLOW-UP AND IDENTIFICATION OF WORST-CASES

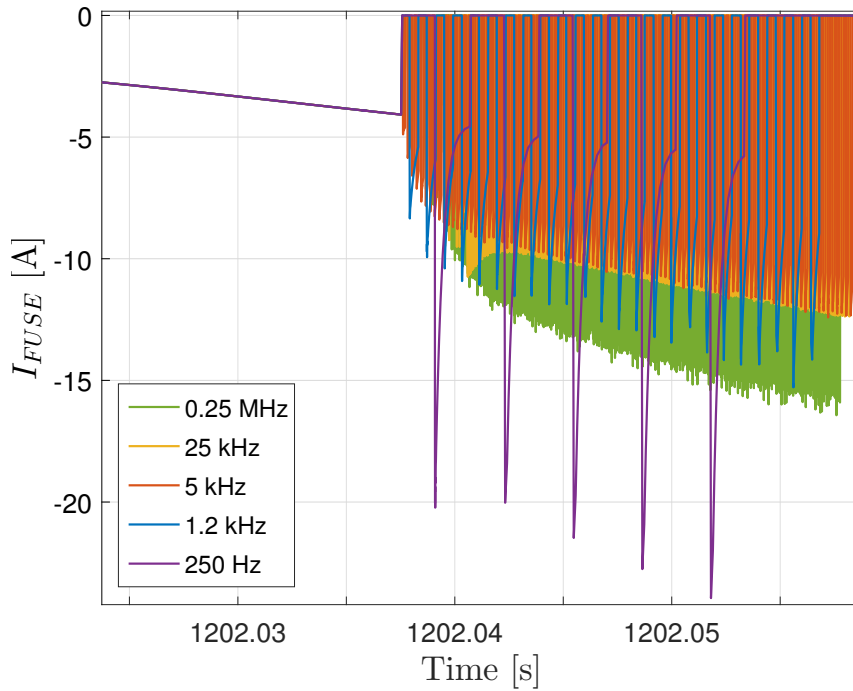


Figure 3.12: Effect of frequency of pulses, occurring after the fuse pre-arcing threshold is reached, on the behaviour of I_{FUSE} for a short of $1\ \Omega$ occurring at magnet 77.

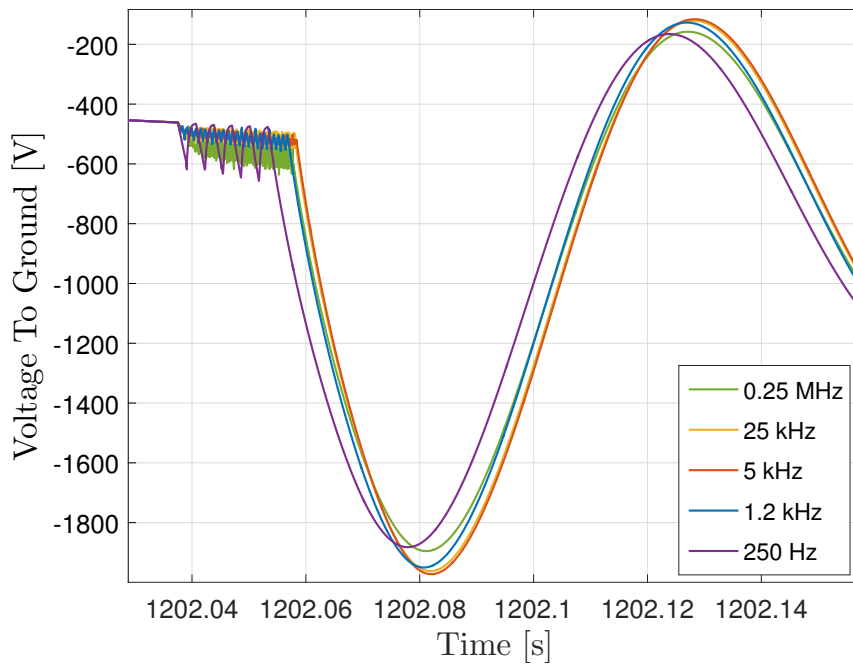


Figure 3.13: Effect of frequency of pulses, occurring after the fuse pre-arcing threshold is reached, on the behaviour of the voltage to ground at magnet 1 with a short of $1\ \Omega$ occurring at magnet 77.

resistance values, allowing for points of interest to be easily identified.

Starting with figure 3.14, a comparison is presented for the peak voltage to ground values obtained from simulations where the fuse did not blow up and the ones where the blow up behaviour of the fuse was implemented. For the latter case shown in figure 3.14b,

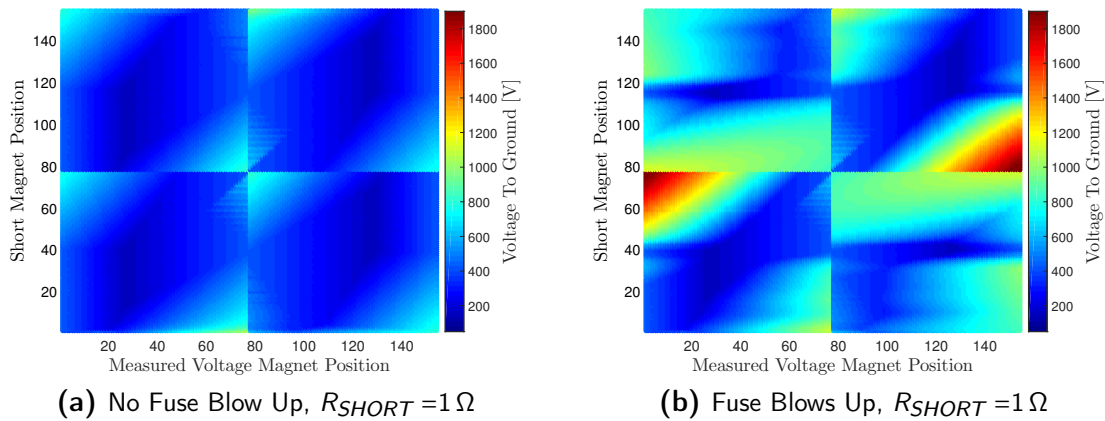


Figure 3.14: Comparison of peak voltage to ground values for a short resistance value of $R_{SHORT} = 1\Omega$ for the case where the fuse never blows up and the one where the blow-up behaviour is included in the simulation.

the magnets in between electrical positions 1 and 30 obtain the peak values for shorts occurring between magnets in positions 57 and 77. Peak values can also be seen for all magnets starting from position 124 up to 154 when the short occurs between magnets 78 and 98. The same pattern for the peak values is maintained in the color plot of the no blow-up case, since the peak voltage is obtained by the same combination of magnet and short position. However, the peak voltages in this case have values almost half the ones obtained in the case where the fuse behaviour was simulated, an expected result since the high values appear during the transient behaviour of the voltage to ground signals following the fuse blow-up, as was previously analysed.

A comparison of the peak voltage values obtained in the case where the blow-up behaviour of the fuse is modeled for different short resistance values is presented in figure 3.15. The similarity of the plots for the short resistance values of $R_{SHORT} = 1\Omega$ and $R_{SHORT} = 10\Omega$ becomes immediately visible. As became clear in figure 3.10a, the voltage to ground reaches its peak value after the fuse has blown up. According to expression 3.2, the value that the equivalent resistance to ground obtains in that case is equal to $10\text{ k}\Omega$. Since the equivalent resistance can be up to 3 orders of magnitude larger than the value obtained by the short, when R_{SHORT} has a value of less than 10Ω , different resistance values belonging in the aforementioned range don't cause a significant change in the peak voltages and the color plot remains the same.

For resistances less than 10Ω , with two values belonging in this range shown in figures 3.15a and 3.15b, high voltage to ground values are reached for magnets in electrical positions 1 to 30 for shorts occurring between magnets 57 to 77 and magnets 124 to 154 for a short in positions 78 to 98. For shorts occurring between positions 30 to 40 and 110 to 120, it can be seen that irrespectively of the magnet position where the voltage to ground is measured, only small values can be obtained for the peak. This is an expected result, since these magnets obtain the lowest voltage drop values even during the absence of a short in the circuit, as was seen in figure 2.6b. The middle range voltage values of about 1 - 1.2 kV are obtained by all magnets up to number 77 in the

3.3. CIRCUIT BEHAVIOUR FOLLOWING FUSE BLOW-UP AND IDENTIFICATION OF WORST-CASES

cases where a short occurs at magnet positions in the range of 78 to 98 and magnets from 78 to 154 when the short occurs at a position in the range of 57 to 77.

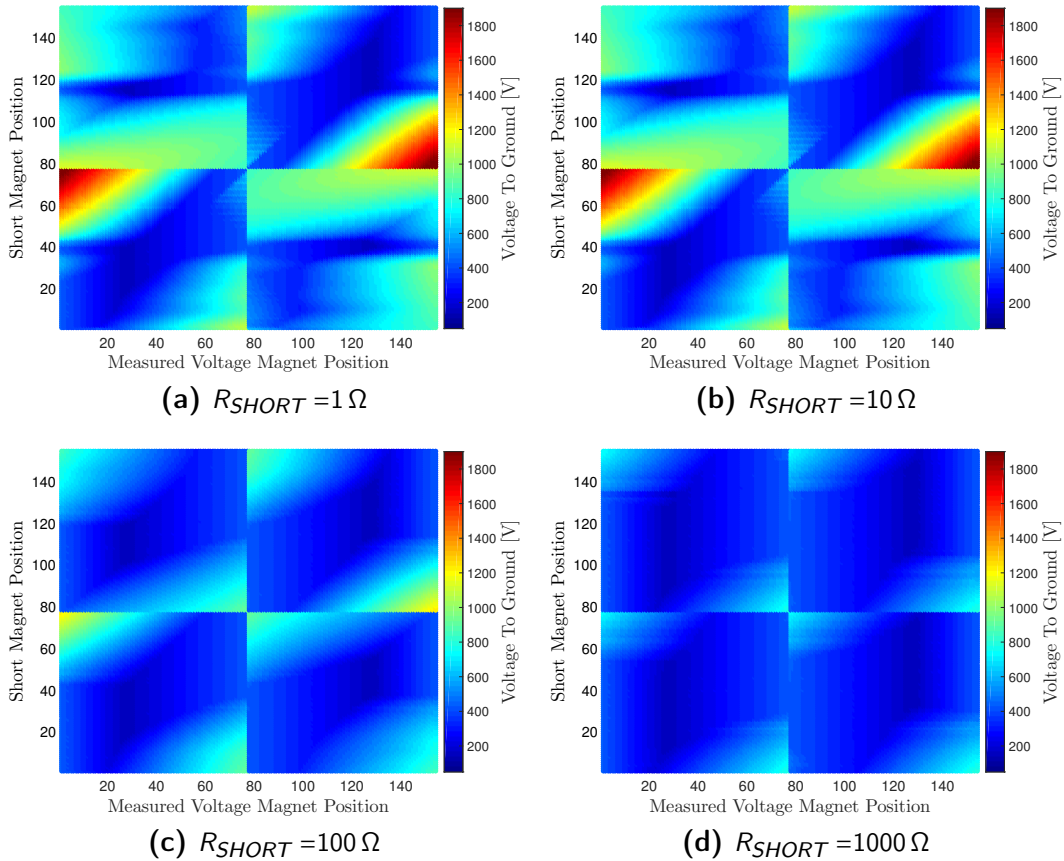
For the case where the resistance of the short is equal to $100\ \Omega$, the color plot is presented in figure 3.15c. For easier reference, the colorbar limits have been kept the same as in the plots of the smaller resistance values, which reveals that for this value of resistance, the voltages to ground in the circuit are significantly smaller when compared to the peak of 1.9 kV. The maximum value obtained in this plot has a value of about 1.3 kV for magnet 154 with a short occurring at position 78. For this resistance value, peak voltages can be seen when the short appears at magnets 57 to 77 for all magnets at positions ranging from 1 to 30, while for magnets at electrical positions 124 to 154 the largest voltage values appear when the short occurs between magnets 78 to 98 and ground. Voltage values in the range of 0.8 kV to 1 kV are obtained for this resistance value at magnet positions 57 to 77 when a short occurs at magnets 1 to 22 and 78 to 90. This is also the case when a short appears at positions 57 to 77 and 140 to 154 for magnets at positions 78-98. Finally, voltages of the same range are observed for magnets in positions 1 to 22 for a short that occurs at magnets 140 to 154 as well as positions 140 to 154 for a short at positions 1 to 22.

The same analysis follows for the plot in figure 3.15d where $R_{SHORT} = 1\text{ k}\Omega$, with the difference that the voltage to ground values have even smaller magnitudes, with the peak voltages reaching values of about 0.9 kV. For high resistance values, the current flowing through the short resistor is limited, which means that the lower values for the voltage to ground obtained are expected.

The above analysis can be summarised in 8 notable cases presented in table 3.2. The table includes the peak values obtained for short resistance values $\leq 10\ \Omega$, where the worst cases are achieved. The table also aims to act as a quick reference for the voltage values obtained for magnets at specific electrical positions, by providing a formula to calculate the peak voltage when the short and magnet positions are within specified ranges.

Table 3.2: Cases Of Peak Voltages To Ground For $R_{SHORT} \leq 10\Omega$

Notable Case #	Short Position	Magnet Position	Voltage Range [kV]	Peak Voltage
1	57-77	1-30	1.7 - 1.9 kV	$2R_{EE}I + \frac{N_{MAG}}{2} V_D$
2	78-98	124-154	1.7 - 1.9 kV	$2R_{EE}I + \frac{N_{MAG}}{2} V_D$
3	78-98	1-77	0.8 - 1.3 kV	$R_{EE}I + \frac{N_{MAG}}{2} V_D$
4	57-77	78-154	0.8 - 1.3 kV	$R_{EE}I + \frac{N_{MAG}}{2} V_D$
5	150-154	1-5	0.1 - 0.8 kV	$R_{EE}I$
6	1-5	73-77	0.1 - 0.8 kV	$R_{EE}I$
7	150-154	78-98	0.1 - 0.8 kV	$R_{EE}I$
8	1-5	150-154	0.1 - 0.8 kV	$R_{EE}I$


 Figure 3.15: Colorplots of voltage to ground peak values as function of magnet electrical position and position where the short occurs for 4 different R_{SHORT} values.

CHAPTER 4

SHORT CIRCUIT ALGORITHM

A thorough analysis of the circuit following the occurrence of a single short to ground has been performed in the previous chapter of this thesis and a better understanding of its behaviour has been achieved. After a short to ground appears in the circuit, the voltage feelers provide the measured voltage to ground signals of the event for 52 of the circuit magnets. Currently, these signals are then obtained and analysed by experts, who provide details regarding the short resistance value and position. The main goal of this chapter is to investigate whether the relation that exists between the fault parameters and the behaviour of the measured signals can be used in order for an automated scheme, able to provide the desired information concerning a short in the circuit, to be implemented. Such an automated solution would greatly reduce the effort currently required to analyse the obtained signals and therefore minimise the total time needed before further details, following a short to ground event, become available.

A first approach that could be used to design the automated scheme, is performing a comparison between the measured voltage to ground signals and simulation results with a short resistance to ground existing in the circuit, since an accurate model of the the main dipole circuit exists [19]. However, in order to obtain the results of the numerical simulations, as already thoroughly discussed, the input parameters of the current in the circuit, as well as the position of the short and its resistance need to be set in advance. This makes clear the fact that performing simulations for a large number of different parameter values is both computationally expensive and time consuming, which defeats the original motivation for the design of the automated scheme.

It has already been seen from plots of the voltages to ground over time, like the one presented in figure 2.6a, that abrupt events in the circuit are followed by transients. However, after these short-term oscillations have died off, the signal values can be defined as a function of the current circulating in the circuit, with the total voltage distributed equally over the magnets of the chain. It is hence suggested that obtaining an analytical solution for the current in the circuit as well as through the short, can lead to an analytical derivation of the voltages to ground.

With a large number of possible values for the initial current and short resistance parameters, the derivation of a system of analytical equations would provide an efficient way to calculate the voltage to ground distribution in the circuit. After taking into consideration certain assumptions and performing simplifications, the LHC main dipole circuit presented in figure 2.3 can be reduced to an equivalent model, that can be solved analytically. Although this equivalent circuit can only be used for the analysis of slow transients, meaning that it is not a substitution of the dipole equivalent model presented in [19], it provides the basis for the derivation of the analytical equations as well as the final algorithm.

4.1 Simplifying the LHC Main Dipole Equivalent Electrical Circuit

During the analysis of the LHC main dipole circuit model, and more specifically referring to table 2.2, it has been mentioned that distributed capacitances to ground are used in order to model parasitic effects. In the case where these capacitances to ground are neglected, the model will show inaccuracies during fast transients, but should still be able to capture the behaviour of the circuit well during slower ones. Since the behaviour of the magnet in the frequency domain is of little interest to this thesis and transients occur occasionally only during abrupt events, a first simplification is applied and the capacitors to ground are removed from the model. The resulting voltage to ground signal for a single magnet and more precisely the one at electrical position 10, is presented in figure 4.1 so that a comparison can be drawn between the case where the capacitors to ground are included and the one they are omitted from the circuit. Although the signal of a single magnet is shown in the figure, the same effect is observed for the voltages of all the other magnets, which is expected since the equivalent model of figure 2.4 is used for all magnets. It becomes visible that the two signals obtained from the case when the capacitors are included in the circuit and the one where they are not, match well, except for the parts where the fast transients occur.

The magnets in the circuit are placed in cryogenic cells, with each cell including either two or three magnets. This is also the reason why a magnet's electrical position does not necessarily correspond to its physical position in the circuit. A table relating the two and showing the magnets included in each cell, is presented in figure A.2 of Appendix A.2. A common grounding point exists for the magnets belonging in the same cell, which depending on its position in the circuit, is connected further or closer to the grounding point of the EE resistor. The distance of the cell from the actual ground point determines the amount of added resistance and inductance to the grounding lines, due to the existence of parasitic resistance and inductance in the connections between the cells. The additional inductance and resistance due to the grounding lines can be calculated using expressions 4.1 and 4.2, where R_{eq} is the equivalent resistance of the grounding lines, which depends on the state of the fuse and is calculated using equation 3.2.

4.1. SIMPLIFYING THE LHC MAIN DIPOLE EQUIVALENT ELECTRICAL CIRCUIT

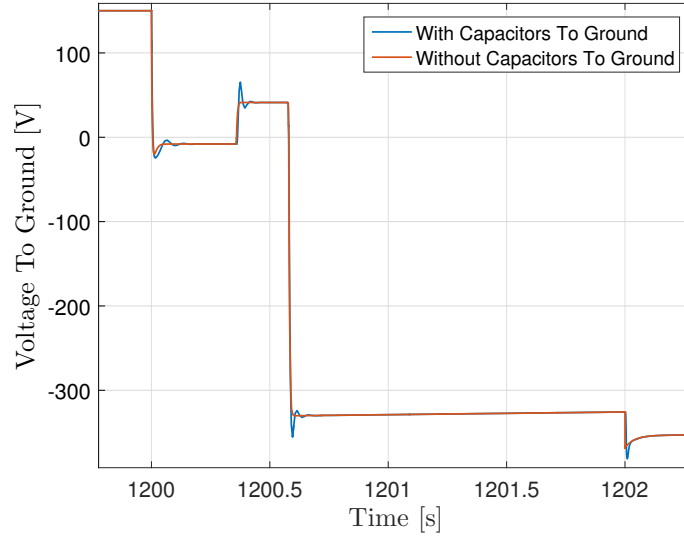


Figure 4.1: Comparison of simulated voltage to ground at magnet in electrical position 10 of the LHC main dipole circuit, showing the effect of the omission of the capacitances to ground in the equivalent model.

$$L_{groundTotal} = CellPositionNumber \cdot 1 \mu\text{H} \quad (4.1)$$

$$R_{groundTotal} = R_{eq} + CellPositionNumber \cdot 3 \text{ m}\Omega \quad (4.2)$$

However, using the formulas it can be seen that even for the case where the cell in position 54 is considered, which has the largest distance from the ground point, the added inductance of the grounding lines is equal to $54 \mu\text{H}$ and the added resistance is equal to 0.16Ω . With the inductance of the magnets being in the order of mH and the resistance of the grounding lines in all cases of equation 3.2 at least two orders of magnitude higher than $\text{m}\Omega$, the additional values of the cell interconnections could be ignored, without significantly affecting the accuracy of the model.

The power supply and the crowbar can be simplified by having a current circulating in the circuit with an initial value at time t_0 . The behaviour of the current over time greatly depends on the total inductance as well as resistance of the circuit. For this reason, accurate values need to be provided for both. The magnets are considered the main inductive elements in the circuit, each having an inductance $L_{mag} = 98 \text{ mH}$. Additional inductance exists at the busbars connecting the different elements of the circuit, however this value is 3 orders of magnitude lower than that of the magnet inductance and can hence be neglected without causing significant deviations of the signal values.

As far as the equivalent resistance is concerned, when the switch connected in parallel to each energy extraction resistor is open, the subcircuit of the EE system can be modeled as a resistor connected in series with the chain of magnets. To increase the accuracy of the equivalent circuit model, the resistances R_{warm1} , R_{warm2} , R_{warm3} and R_{warm4} of the warm copper cables are also included. R_{warm1} models the resistance that exists between the output of the power converter and the magnet in electrical position 1 and has a value of $775.5 \mu\Omega$. R_{warm2} and R_{warm3} both have a value of $69.5 \mu\Omega$ and represent the

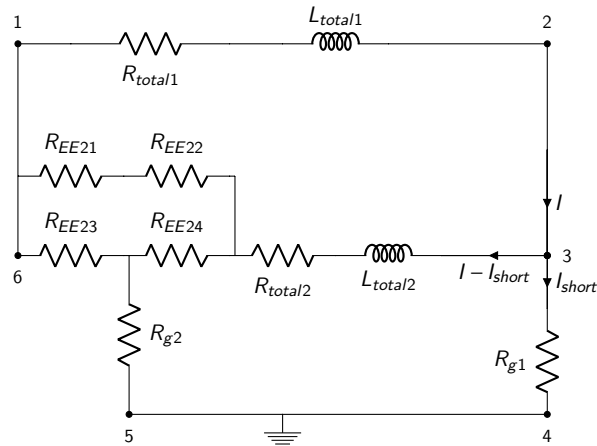


Figure 4.2: Equivalent model of the LHC main dipole circuit for slow transients in the case where a short to ground has occurred.

resistance in either side of the EE1 resistor. Finally, R_{warm4} can be found between magnet 154 and the EE2 resistor and has a value of $428.5 \mu\Omega$. Since the total value of the warm resistance adds up to approximately $1.5 \text{ m}\Omega$, it has to be added to the energy extraction resistances in order to obtain an accurate value for the equivalent circuit resistance.

Taking into consideration all the simplifications discussed above, a reduced equivalent circuit that models the behaviour of the LHC main dipole circuit during slow transients is created and presented in figure 4.2.

In the schematic shown in the figure, the short circuit exists at node 3, which constitutes the connection point between a specific magnet and ground. The inductances and resistances that exist before and after the short position are lumped together and represented by L_{total1} , L_{total2} and R_{total1} and R_{total2} respectively. The equivalent ground resistance R_{g2} connects to the middle point of EE2 and is effectively in series to the ground resistor R_{g1} .

4.2 Analytical Solution of Reduced Equivalent Circuit Model

The circuit has now been simplified to a network of resistors and inductors. Three distinct circuit loops can be seen and an equation can be derived for each. Since having an expression for the current through resistors R_{EE21} and R_{EE22} is not required in order to calculate the current through the short resistor, a further simplification can be applied to the circuit. The Wye-Delta transform [23] can be performed on the branch of the second EE resistor, with the aim of obtaining one common node for the resistors that make up R_{EE2} . The additional simplification of the reduced equivalent circuit after the transformation has been applied, is presented in figure 4.3. A complete calculation of the resistances resulting from the transform that leads to the final schematic of the reduced circuit, is presented in Appendix A.1. An elaborate explanation of all the resistive and

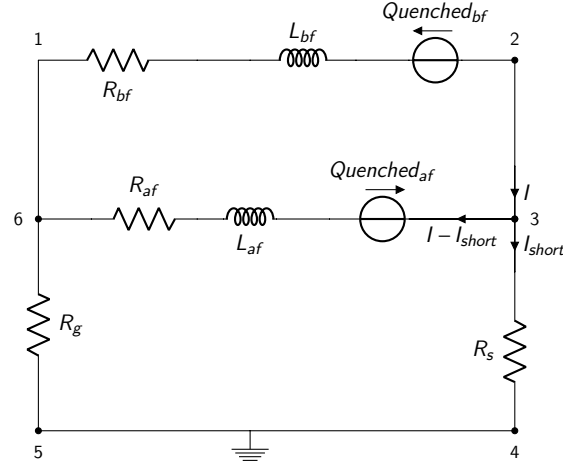


Figure 4.3: Further simplification of the reduced model using the Wye-Delta transform on the EE2 resistor branch.

inductive components included in the circuit schematic as well as their values is given in this section.

The total inductance and resistance of each loop depends on the electrical position of the magnet where the short occurs. As an example, for a short that appears between magnet 70 and ground, the total inductance before the position of the short is equal to $L_{bf} = 69L_{mag}$, while the inductance following the short position is equal to $L_{af} = (154 - 69)L_{mag}$. Similarly, since magnet 70 is positioned before the EE1 resistor, the total resistance preceding the short position is equal to $R_{bf} = R_{warm1} + R_1$ and the total resistance after the short equal to $R_{af} = R_{warm2} + R_{warm3} + R_{warm4} + R_{EE2} + R_2$, where R_1 and R_2 are the resistors resulting from the transform, as specified in Appendix A.1. Therefore, it becomes possible for the values of these parameters to be computed programatically, given the position of the magnet where the short occurred.

Generalised for every possible short position, the formula for the calculation of the total resistance R_{bf} can be seen in 4.3, while the one for R_{af} in equation 4.4. The equivalent resistances R_1 and R_2 , derived using the Wye-Delta transform in Appendix A.1, are also included in the following equations.

$$R_{bf} = \begin{cases} R_{warm1} + R_1, & \text{if shortPosition} \leq 77 \\ R_{warm1} + R_1 + R_{EE1} + R_{warm2} + R_{warm3}, & \text{if shortPosition} > 77 \end{cases} \quad (4.3)$$

$$R_{af} = \begin{cases} R_{EE1} + R_{warm2} + R_{warm3} + R_{warm4} + R_2, & \text{if shortPosition} \leq 77 \\ R_{warm4} + R_2, & \text{if shortPosition} > 77 \end{cases} \quad (4.4)$$

In a realistic situation, it can be the case that quenched magnets exist in the circuit. When this happens, the voltage drop across a quenched magnet is equal to the voltage drop over the diode connected in parallel, through which the magnet is bypassed. More specifically, the voltage value becomes equal to 6 V in cryogenic conditions and

approximately 1.2V after heating up, as has been previously shown in figure 2.2. Neglecting the time needed for the lower voltage to be obtained, the voltage drop over the quenched magnet can be considered as having a constant value. This is the reason that the quenched magnets are represented as voltage sources $Quenched_{bf}$ and $Quenched_{af}$ in figure 4.3, for the magnets that have quenched before and after the short respectively. The formula to calculate the voltage value of each source is presented in equations 4.5 and 4.6.

$$Quenched_{bf} = NumberOfQuenchedMagnetsBeforeShort \cdot 1.2V \quad (4.5)$$

$$Quenched_{af} = NumberOfQuenchedMagnetsAfterShort \cdot 1.2V \quad (4.6)$$

From the above equations, it becomes clear that the electrical positions of the magnets that have quenched are required as input, in order to create an accurate representation of the state of the circuit at a specific time. This information can easily be obtained in a real scenario, since the quench detection system installed in the LHC main dipole circuit records the voltages across the magnets that triggered it.

As a result of representing a quenched magnet by a voltage source, the inductances L_{bf} and L_{af} need to be decreased by a number that depends on whether the quenched magnet is found before or after the position where the short occurred. Taking into consideration the existence of quenched magnets in the circuit, the analytical expressions for L_{bf} and L_{af} , generalised for all possible short positions, are presented in equation 4.7 and 4.8 respectively. In these equations, the variable $shortPos$ represents the magnet number where the short occurred and N_{mag} is the total number of magnets in the circuit.

$$L_{bf} = (shortPos - 1 - NumberOfQuenchedMagnetsBeforeShort)L_{mag} \quad (4.7)$$

$$L_{af} = (N_{mag} - (shortPos - 1) - NumberOfQuenchedMagnetsAfterShort)L_{mag} \quad (4.8)$$

The short resistor R_s can be seen connected to ground and effectively in series to R_g , which represents the total resistance of the grounding subcircuit, presented in figure 3.7. The series connection of the two resistors obtains the values presented in expression 3.2, analytically discussed in section 3.2. Another simplification is made in the model regarding the above mentioned expression. More specifically, since the model does not take into account the time dependent behaviour of the elements, the resistance of R_g can be considered as having a value of $R_g = 8.66\Omega + R_3$, where R_3 is the resistor inserted in series as a result of the Wye-Delta transform (Appendix A.1). This means that the time needed for the 15V threshold of the ground diodes to be reached, which was used as a condition in equation 3.2, is neglected. Since the resistors R_s and R_g are effectively in series, without loss of generality it is possible to keep the value of resistor R_g constant and account for a potential blow up of the fuse using resistor R_s , which would obtain a high value in that case.

Following the simplification of the EE2 branch, two loops passing through the nodes $1 \rightarrow 2 \rightarrow 3 \rightarrow 6$ and $3 \rightarrow 6 \rightarrow 5 \rightarrow 4$ can be defined in the circuit. A solution needs to be found for the two unknown variables in the circuit, namely I and I_{short} , with the first

4.2. ANALYTICAL SOLUTION OF REDUCED EQUIVALENT CIRCUIT MODEL

being the current circulating in the circuit before the short position and the latter, the current through the short. With a known value of the ground resistor R_g and a solution obtained for I_{short} , it then also becomes possible to calculate the voltage to ground of the magnet at which the short occurred.

Applying Kirchhoff's voltage laws to the two aforementioned circuit loops, the circuit behaviour can be described using two differential equations. The built-in ODE solver of *MATLAB* can then be used to provide the analytical solution of their system. The differential equation for the first loop is shown in equation 4.9 and for the second one in equation 4.10. Initial values are defined as $I(t_0) = I_0$ for the circuit current and $I_{short}(t_0) = 0$ for the current through the short resistor. The complete analytical solutions of the system for the variables I_{short} and I are presented in Appendix A.3, while the expressions of the σ variables included in the solutions are shown in figures A.4 and A.5.

$KVL_{1 \rightarrow 2 \rightarrow 3 \rightarrow 6}$:

$$R_{bf} \cdot I + L_{bf} \cdot \frac{dI}{dt} + R_{af} \cdot (I - I_{short}) + L_{af} \cdot \frac{d}{dt}(I - I_{short}) + Quenched_{bf} + Quenched_{af} = 0 \quad (4.9)$$

$KVL_{3 \rightarrow 6 \rightarrow 5 \rightarrow 4}$:

$$L_{af} \cdot \frac{d}{dt}(I - I_{short}) + R_{af} \cdot (I - I_{short}) + I_{short}(R_s + R_g) + Quenched_{af} = 0 \quad (4.10)$$

Having obtained a solution for both current values in the circuit, it becomes possible to calculate the voltage drop over the magnets both before and after the short, as presented in equations 4.11a and 4.11b respectively.

$$U_{mag_{bf}} = L_{mag} \frac{dI}{dt} \quad (4.11a)$$

$$U_{mag_{af}} = L_{mag} \frac{d(I - I_{short})}{dt} \quad (4.11b)$$

Finally, the voltage to ground at each magnet position can be calculated using equations 4.12, 4.13, 4.14 and 4.15, with *MagnetNumber* a variable representing the electrical position of the magnet for which the voltage is defined.

$$U_{ground}(1) = \begin{cases} U_{mag_{bf}}, & \text{if } shortPosition < 1 \\ U_{mag_{af}}, & \text{if } shortPosition > 1 \end{cases} \quad (4.12)$$

$$U_{ground}(78) = \begin{cases} U_{mag_{bf}} + R_{EE1}I, & \text{if } shortPosition < 78 \\ U_{mag_{af}} + R_{EE1}I, & \text{if } shortPosition > 78 \end{cases} \quad (4.13)$$

$U_{ground}(MagnetNumber) =$

$$= \begin{cases} U_{ground}(MagnetNumber - 1) + U_{mag_{bf}}, & \text{if } MagnetNumber < shortPosition \\ U_{ground}(MagnetNumber - 1) + U_{mag_{af}}, & \text{if } MagnetNumber > shortPosition \end{cases} \quad (4.14)$$

$$\begin{aligned}
 U_{ground}(MagnetNumber) &= \\
 &= U_{ground}(MagnetNumber - 1) + 1.2, \text{ if } MagnetNumber \text{ is quenched}
 \end{aligned}
 \tag{4.15}$$

A first comparison between the current through the short (I_{short}) values calculated analytically and the signal obtained from the simulation of the complete model, is presented in figures 4.4 and 4.5 for two different orders of magnitude of the short resistance value, namely 1Ω and 100Ω .

For the short event presented in both figures, it is considered that the short occurred between magnet 70 and ground. Additionally, the value of the current in the circuit at the time the short occurred was 11.32 kA and no magnets were quenched. The analytical solution was computed in about 7 s , while the numerical simulation in *PSpice* required about 16 s to complete. It is important to mention that the same time grid was used in both simulations, which included 2000 equally spaced points between values 0 s to 400 s . Although an increase of the grid's resolution requires additional computational time, the analytical solution was repeatedly computed in approximately half the time of the numerical simulation. The main reason for this, is the fact that *PSpice* executes the simulation for certain initially specified parameters, while on the other hand the analytical solution of the differential equation contains symbolic variables for the different parameters. As a result, computing the values of the current, after a change of parameters has taken place, requires about 5 s , while on the other hand the time *PSpice* needs to complete the simulation remains the same.

Looking at the figures, it can easily be seen that the signals overlap better for certain time regions than others. In order to obtain a value for the similarity of the two curves,

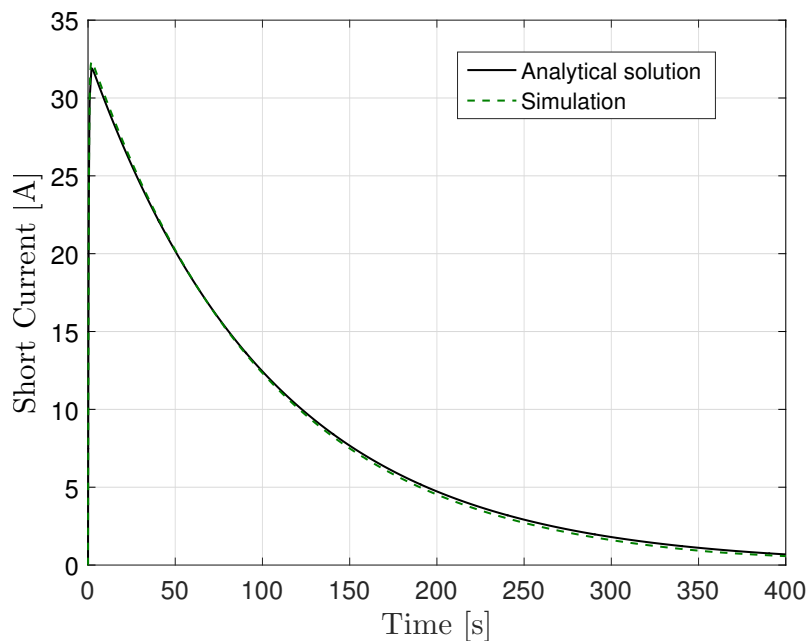


Figure 4.4: Comparison of simulated and analytically computed signal of the current through the short when it occurs between magnet 70 and ground with a resistance value of 1Ω .

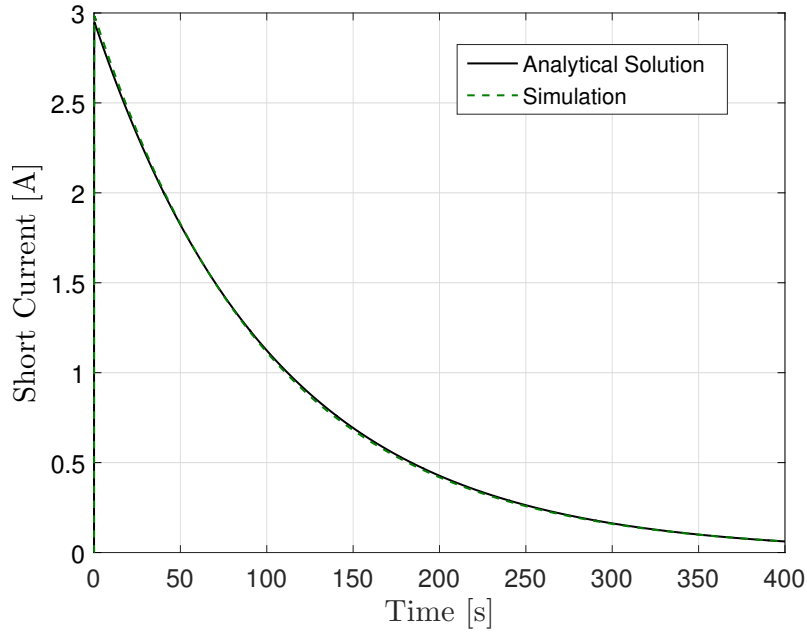
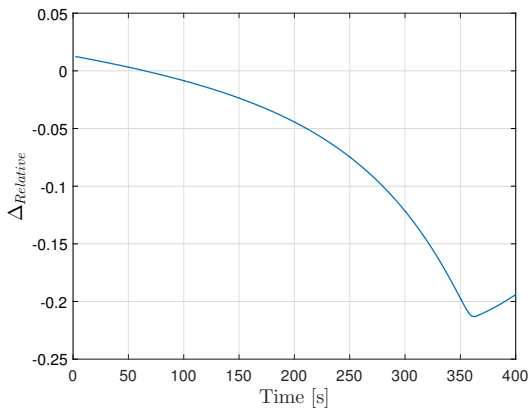


Figure 4.5: Comparison of simulated and analytically computed signal of the current through the short when it occurs between magnet 70 and ground with a resistance value of 100Ω .

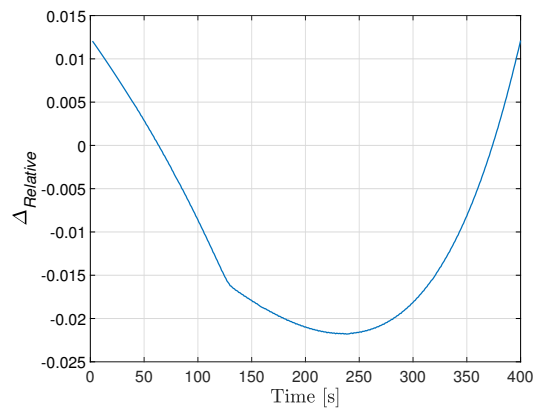
their relative difference is calculated by averaging the distance values of their individual data points. In order to achieve this, the signals are first interpolated and the formula presented in 4.16 is used.

$$\Delta_{Relative} = \frac{1}{N_{datapoints}} \sum_{i=1}^{N_{datapoints}} \frac{|(I_{simulated}_i) - (I_{analytical}_i)|}{|I_{simulated}_i|} \quad (4.16)$$

The relative difference is plotted as a function of time in figures 4.6a and 4.6b for each short resistance value respectively. With a resistance of 1Ω , it can be seen that the



(a) Relative distance of simulated and analytical solution of I_{short} with a short resistance of 1Ω plotted against time.



(b) Relative distance of simulated and analytical solution of I_{short} with with a short resistance of 100Ω plotted against time.

Figure 4.6: Relative distance between simulated and analytically computed data points of the current through the short, plotted against time for two different short resistance values.

Table 4.1: Maximum and Mean Absolute Values of the Relative Difference Between Simulated and Analytically Calculated Current Through the Short Signals for Different Short Resistance Values.

R_s [Ω]	Max Relative Distance	Mean Relative Distance
1	0.213	0.028
100	0.021	0.005

relative error obtains values less than 2% up to 150 s, after which the absolute difference value continues increasing and eventually reaches a maximum of about 21%. For the case where the resistance of the short is equal to 100 Ω , the error has an average absolute value of less than 1%, with a peak value of approximately 2%. The absolute values of the maximum and mean relative distance, obtained for both resistance values, are presented in table 4.1.

A possible cause for the higher error values observed for times larger than 150 s, in the case of the smaller short resistance, could be the fact that the equivalent resistance of the grounding lines does not maintain a constant value and instead as the current decreases, the diodes in parallel to the fuse resistor stop conducting, causing hence an increase of the equivalent resistance value. Overall however, it can be said that the analytical solution that is obtained for the currents in the circuit, represents with high accuracy the circuit behaviour. This means that the analytical derivation of the voltage to ground values for the magnets in the circuit, as explained in this section, can constitute the basis for the automation scheme to be developed. Since the higher error values are obtained after a certain time following the zero point, this can be a point taken into consideration for the results provided by the automated scheme when later time points are used.

4.3 Design of Short Circuit Algorithm

In the previous section, equations for the voltage to ground values of the reduced equivalent circuit magnets were presented, which make use of the analytical solutions of the current in the circuit as well as the current through the short. Expressions have also been provided for the calculation of the lumped element values that exist in the equivalent circuit, which require knowledge of the short position and the number of quenched magnets.

An algorithm can hence be proposed that compares the analytically calculated voltage to ground values for each magnet in the circuit to the measured ones and draws conclusions about the short position and resistance value. More specifically, it calculates the mean distance value between the measured voltages to ground of the magnets provided by the voltage feelers and the analytically calculated ones at a specified time. The algorithm takes advantage of the reduced time needed to compute the result of the analytical expressions of the currents and calculates the voltage to ground values for all

154 possible short positions as well as several short resistance values. It finally identifies the voltage values for which the minimum distance is obtained and returns the corresponding short position and resistance values as output. A more detailed description of the steps followed by the algorithm in order to provide information regarding the short, follows next.

As a first step, the total number of magnets, the values of the warm resistances R_{warm1} , R_{warm2} , R_{warm3} and R_{warm4} and magnet inductance L_{mag} as well as the values of the EE resistors R_{EE1} , R_{EE2} are provided as inputs to the algorithm. Having these values specified as inputs is important for two main reasons. The first is the fact that the above mentioned resistance parameters model resistors that in the actual circuit tend to deviate from their specified nominal value, with their values even changing completely in the case they are replaced by different resistors. Second, leaving the freedom of manually inserting such parameters does not limit the proposed algorithm only to the LHC main dipole circuit, but makes it compatible with other accelerator circuits, which have different EE resistor and magnet inductance values or a different total number of magnets. The positions of the magnets that quenched, as well as the times at which each quench occurred are also provided to the algorithm.

The second set of inputs to the algorithm consists of the measured signals that have been obtained during the short to ground event. The high resolution data signal of the circuit current is stored in the Post-Mortem System [15], while the voltage feeler data signals of the event are found in the LHC Logging System [24]. The data can be accessed using queries that include the sector and magnet name as well as the timestamp of the event. The voltage to ground signals are recorded by the voltage feeler sensors, connected to one every three magnets in the circuit, meaning that the voltages to ground of 52 out of the 154 magnets are measured. A list containing their exact position in the circuit and the electrical position of the magnets to which they are connected to, can be found in [25]. The measured signals are sampled with a frequency of 10 Hz, which works well for obtaining the general behaviour of the signal, but is at the same time not able to accurately capture all features of fast transients occurring in the circuit.

The fact that the signals of the circuit current and the voltage to ground are obtained from different systems and have different sampling frequencies, means that synchronisation needs to take place. This can be achieved by shifting both signals accordingly so that the time when the FPA occurs is positioned at $t = 0$ s. Their analysis hence becomes easier, as it is possible to identify the corresponding datapoints in both signals using a common time instance. A method is provided next for the algorithm to identify the time when the FPA is triggered in each of the signals.

As has been previously analysed, the current in the circuit follows an initial ramp-up to its nominal value with a constant $\frac{dl}{dt}$, after which it reaches a plateau. This means that the instant when the FPA is triggered can be identified by the algorithm as the point when the ramp up rate of the current obtains a value close to zero. In the absence of faults in the circuit, the behaviour of the signals is not characterized by sudden changes, apart from the region where the FPA occurs. The points where abrupt changes of the voltage to ground signals occur, can be identified by calculating the numerical derivative

of the signals, which reaches its peak values at those points. The time point at which a first peak in the derivative is detected and which is followed by two other peaks for t_{EE1} and t_{EE2} is characterised as t_{FPA} . The second criterion, regarding the two follow-up peaks, is essential in order to differentiate between the peak of FPA and a different one caused by a short in the circuit. After the peaks for t_{FPA} , t_{EE1} and t_{EE2} have been identified, the rest of them specify the times when a short to ground occurred.

As has been thoroughly discussed in the previous section, obtaining accurate values for the analytical solution of the circuit current I depends on the equivalent resistance of the circuit, which consists of the values of the two EE resistors as well as the warm resistances. Therefore it becomes important that the values of the resistors used in the model, do not deviate much from the ones that exist in the circuit. In case of a mismatch, for a specific value of current at the circuit, an error would appear between the calculated and the measured voltage to ground values for each magnet, even if the correct values for the short parameters were to be chosen. Since the algorithm looks for the closest fit between the calculated and measured voltage values, this could cause incorrect conclusions to be drawn.

In figure 4.7 the effect of changing the EE resistance values on the obtained voltage distribution curves, which are the larger contributor to the total equivalent circuit resistance, is shown. The voltage to ground values plotted in the figure are computed using the analytical expressions with the short occurring at magnet 149 and a short resistance of $0.1\ \Omega$. A linear behaviour relation can be seen existing between the values of the resistances and the voltage distribution, with the slope of the curve becoming steeper as the total voltage in the circuit increases. Since an analog circuit is considered, it can be said that a combination of resistances which minimises the distance of a certain voltage distribution curve from a reference one exists. The error, defined as a function of resistances R_{EE1} and R_{EE2} , can hence be considered continuous. The reference curve to be used for the minimisation problem will consist of the measured voltage to ground values at a specific time after the second EE and before the first short occurs, since no disturbances affect the voltages during that period. The analytically calculated voltage values for the chosen time will be optimised so that their distance to the measured ones becomes minimum. Therefore, a better match of the resistances used in the model with the values in the circuit can be achieved.

A scheme based on the Newton–Raphson method [26] can then be used to find the roots of the error function. An initial guess is made for the two resistance values, which in this case is equal to their nominal values and the total error of the voltages to ground is calculated. The value of the resistance to be used in the second iteration, as well as the ones that follow, can be calculated using equation 4.17, with the numerical derivative of the error function shown in equation 4.18. These formulas are a function of the resistance and error values obtained during previous iterations and will be computed iteratively until the error value shows only small changes for successive iterations, which signifies that convergence has been reached.

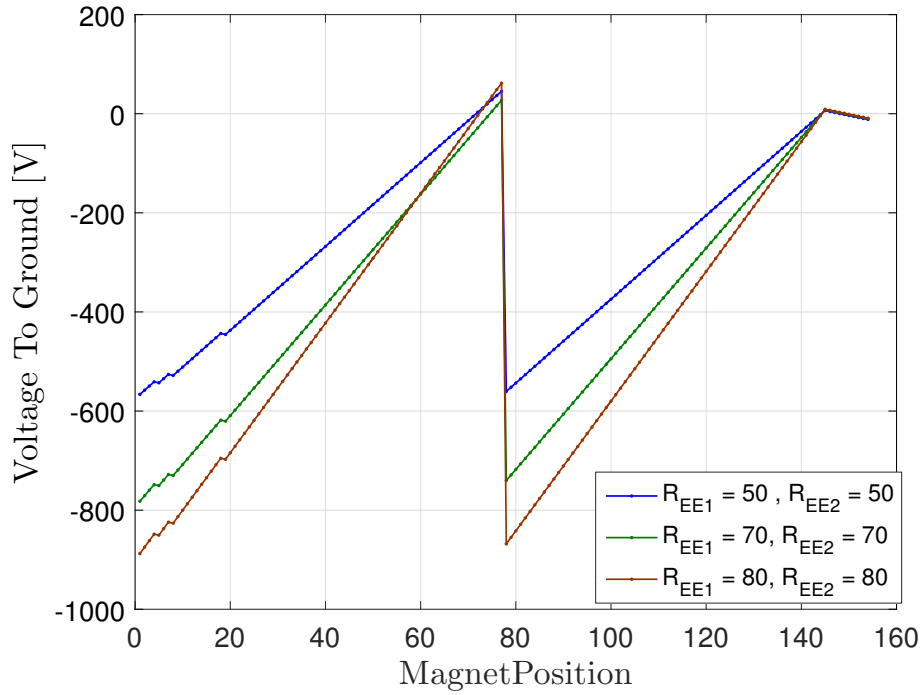


Figure 4.7: Shift of analytically computed voltages to ground for different values of the energy extraction resistors.

$$R_i = R_{i-1} - \frac{\text{error}(R_{i-1})}{\text{error}'(R_i)} \quad (4.17)$$

$$\text{error}'(R_i) = \frac{\text{error}(R_{i-2}) - \text{error}(R_{i-1})}{R_{i-2} - R_{i-1}} \quad (4.18)$$

Two different methods can be used to compute the error function, namely the ℓ^1 -Norm and the ℓ^2 -Norm metric [27]. The formulas used for the case of the voltage to ground signals are presented in equations 4.19 and 4.20, for each norm respectively. It is expected that the two methods will have different convergence rates, which is difficult to estimate however, since the shape of the error function is not known in advance. For this reason, further analysis will be provided for the two metrics during a case study in the next section of the thesis. Both methods will be implemented in the algorithm, so that if convergence is not reached after 10 iterations using one of them, an alternative method exists.

$$\text{error} = \sum_{r=1}^{N_{\text{VoltageFeelers}}} |V_{\text{measured}}(r) - V_{\text{analytical}}(r)| \quad (4.19)$$

$$\text{error} = \sqrt{\sum_{r=1}^{N_{\text{VoltageFeelers}}} |V_{\text{measured}}(r) - V_{\text{analytical}}(r)|^2} \quad (4.20)$$

Following the input of the initial parameters and the optimisation of the resistance values, the differential equations for the two circuit loops are solved. The resulting an-

analytical solutions for the currents are then saved, with the resistance and inductance parameters both before and after the short position as well as the initial current in the circuit kept as symbolic variables in the final solutions of I and I_{short} . This allows for the values of the currents to be quickly computed for various parameters, which can be easily substituted in the expressions without the need of solving the differential equations every time. In order to calculate the solution, the time vector of the measured signals is used, so that the analytical solutions can also be synchronised with the measured data, as previously discussed. In order to compute the solutions for a specific short, a time of about 1 s after its occurrence is chosen, at which the transient oscillations have died off and which is defined as t_0 . The value of the current in the circuit at the chosen time is also obtained and set as the initial current I_0 in the differential equation system.

The algorithm is then able to perform a parametric sweep of the short resistance, which is one of the free variables in the analytical equations. Since obtaining the results for an infinite number of resistance values is not realistic, values at different orders of magnitude are chosen for the sweep and more specifically [0.1, 1, 10, 100, 1000, 10000] Ω . As was previously mentioned, resistor R_g , which represents the total resistance of the grounding subcircuit, is assigned a constant value in the model, which means that it is a change in the value of the short resistor that has an effect on the equivalent resistance of the grounding part of the circuit. Therefore, a short resistor of a large value models the case when the fuse has blown up.

The voltage to ground values for the magnets in the 52 positions where the voltage feelers are located, are calculated analytically for the specified time after the short occurred and for each short resistance value. In order to provide a conclusion for the short resistance of the event, the algorithm needs to identify the specific resistance value for which the average distance of the measured and calculated voltages to ground obtain the smallest value. Due to the fact that another free parameter, namely the position of the short, exists in the analytical solutions, the values need to be calculated for all 154 possible short to ground positions. However, from the analysis performed in the first part of the thesis, it follows that for a fixed short resistance value, the peak voltages to ground are obtained when the short occurs on the first and last magnet of the chain as well as the magnets before and after the EE1 resistor. In order to keep the total computational time requirements low, it is sufficient to check whether the measured voltage values fall in between the minimum and maximum voltages obtained during the worst case scenarios for the specific magnet position.

The method that the algorithm uses in order to determine the mean error between the analytical and measured signals of the 52 magnets is discussed next. Visually this process can be described as a comparison of the distance between two of the curves plotted in figure 3.4. Computing the relative mean difference would provide a better understanding of how much the analytically calculated values deviate from the measured ones, while taking into consideration the scale of the voltage values. However, such a method is not ideal for the comparison of the measured and analytical voltages in this case, since for specific magnets, values around zero are obtained. When this is the case, the relative difference does not provide a valid comparison, since its value tends to high values.

As an alternative, the algorithm calculates the mean absolute difference between the voltages at each of the measured magnet positions where the i_{th} voltage feeler is placed and computes the mean distance for a specific short position and short resistance value by dividing their sum by the total number of voltage feelers. An expression is presented in equation 4.21, where $N_{VoltageFeelers}$ is the total number of voltage feelers, or equivalently magnets for which measured signals exist.

$$\Delta_{Absolute} = \frac{1}{N_{VoltageFeelers}} \sum_{i=1}^{N_{VoltageFeelers}} |(V_{measured_i}) - (V_{analytical_i})| \quad (4.21)$$

Having defined the chosen distance metric for the circuit voltage distributions, the description of the identification process of the short resistance value can be completed. If the mean absolute distance calculated for any of the 4 chosen short positions for a certain resistance obtains a small value, then the specific resistance value can be considered as belonging in the same range as the short resistance of the circuit. In the case where a small distance value is obtained for multiple resistances, then the algorithm considers the smallest and largest of these and returns a range of possible short resistance values for the short.

For the resistance values that the algorithm identified as belonging to the same range as the short resistance of the event, the voltage values for all 154 possible short to ground positions are computed. The mean absolute difference, presented in equation 4.21, is again used for the comparison of the analytical solution values with the measured ones and the magnet electrical position that results in the smallest difference is considered as the one where the short occurred.

The steps followed by the algorithm, are summarised next.

Short Circuit Algorithm

- 1: **procedure** PROVIDE SHORT TO GROUND INFORMATION
 - 2: Input: circuit parameters
 - 3: Input: positions of quenched magnets and time at which they quenched
 - 4: Input: measured data of event (current I_{FPA} , voltages to ground)
 - 5: Find t_{FPA} for both signals and synchronise
 - 6: Optimise model for resistances R_{EE1} and R_{EE2}
 - 7: Solve differential equation and save resulting analytical equations
 - 8: Find range where resistance belongs by identifying resistance values for which minimum distance between measured and calculated voltage values is achieved for the 4 short positions where extreme values are reached
 - 9: Identify value of short position for which minimum distance between measured and calculated voltages is obtained
 - 10: **end procedure**
-

4.4 Testing of Algorithm And Results

As a first case study of the application of the short-circuit algorithm, the event which occurred in a dipole magnet of *Sector 34* on 08/12/2016 is chosen. An investigation following the detection of the specific event by analysing measured signal data recorded on the specified date as well as simulation results, has been presented in [28]. After the event, the electrical quality assurance team performed onsite visits in order to accurately locate the fault, eliminate it and perform specialised measurements. Further details on the event, such as the short resistance and its precise cause, have been provided following the onsite measurements and are detailed in [29]. Using this information, a first validation of the proposed algorithm can be performed and its accuracy when measured signal data are provided as input can be determined.

It has been identified that the short occurred between magnet *C12L4* and ground, which translates to the magnet at electrical position 149 of *Sector 34*. Regarding the exact point where the short occurred, using specialised diagnostic techniques [30], the short to ground was located at the bypass diode connected in parallel to magnet *C12L4*. A value of approximately $0.47\ \Omega$ was determined for the resistance of the short [29]. Finally, although it has been reported that the fuse in the circuit did blow up, the exact time when this occurred is not known [30].

For the specific event, several magnets in the circuit quenched at times both preceding and following the occurrence of the short. The magnet positions as well as the current levels at which the magnets quenched are shown in table 4.2 and are provided as input to the algorithm. With the information regarding the current level at the time when the short occurred known, it can be seen that 4 out of the total 22 magnets quenched before the occurrence of the short, namely the magnets in electrical positions 5, 19, 149, 150.

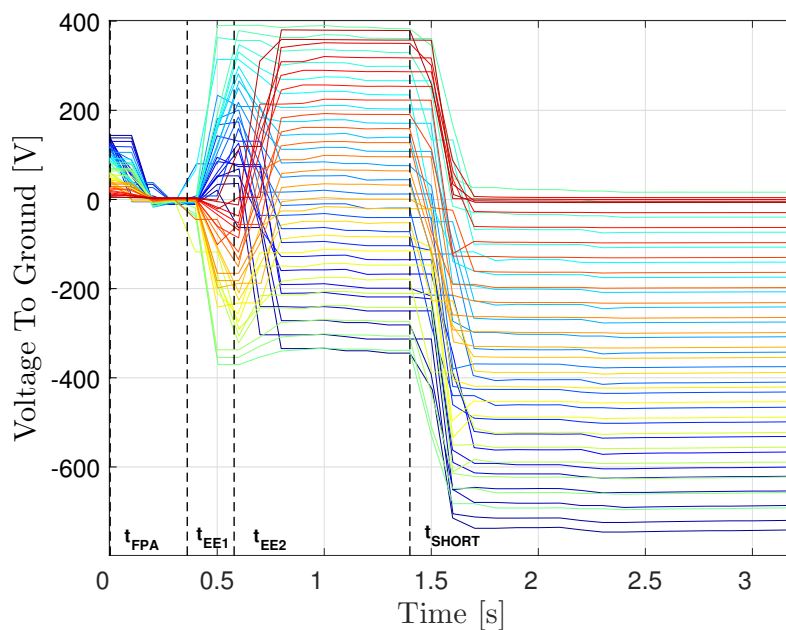


Figure 4.8: Measured voltage to ground signals of 52 magnets obtained from the incident of 08/12/16.

Table 4.2: Quenched Magnets And Value of Circuit Current When Quench Occurred

Before Short	Magnet Electrical Position	I_{QUENCH} [A]
YES	19	11416
YES	149	11415
YES	150	11374
YES	5	11359
NO	148	11297
NO	146	11296
NO	147	11296
NO	151	11293
NO	154	11293
NO	153	11293
NO	152	11281
NO	8	11280
NO	3	11205
NO	7	9176
NO	6	9170
NO	4	8456
NO	2	8452
NO	1	8452
NO	136	7313
NO	18	3933
NO	9	3833
NO	135	2460

The voltage to ground signals for the specific event have been obtained from the LHC Logging Database and are plotted in figure 4.8. Comparing the measured signals of the figure to the simulated voltages to ground shown in figure 3.3a, where a single short to ground existed in the circuit, the effect of the low sampling frequency becomes visible in the fast transient regions. Although it is not possible to obtain an accurate voltage value for a time point in between the two EE switch openings, due to a lack of data points, the times at which these events occur can still be identified, since the behaviour of the signals is well understood. The times of the 3 events occurring during the FPA are indicated by dashed lines in figure 4.8. After the second EE switch opens in the circuit, the voltages are expected to slowly decay to zero with an almost exponential rate. An abrupt change that occurs after this event, can hence be characterised as a short circuit. For the specific event, it becomes visible in the same figure that the short appears approximately 1 s after EE2, with the current in the circuit at the specific moment having a value of about 11.31 kA.

Next, the 52 measured voltage to ground signals are provided as input to the algorithm.

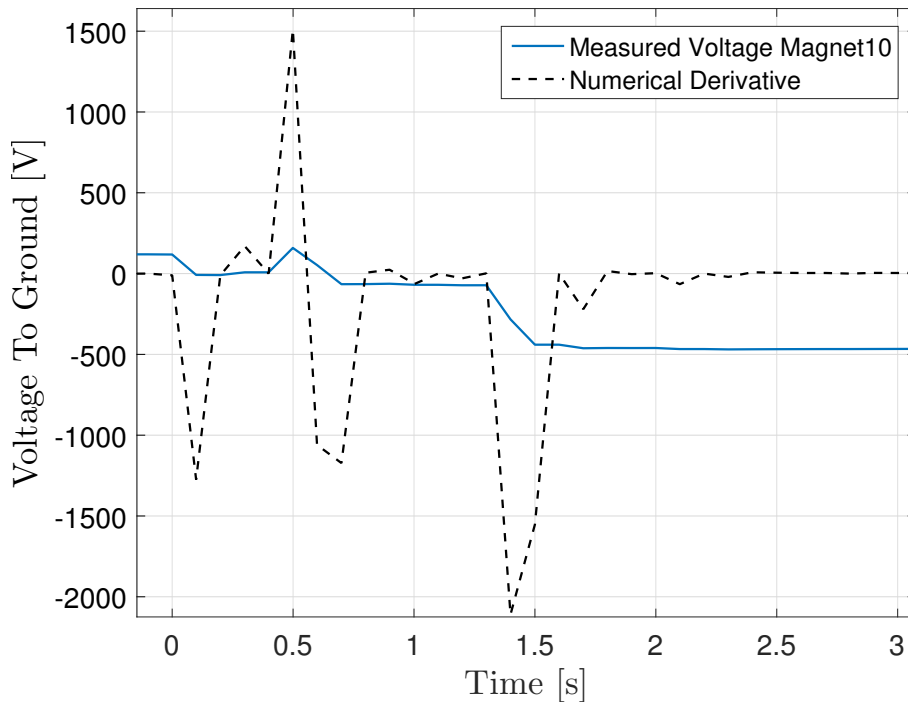
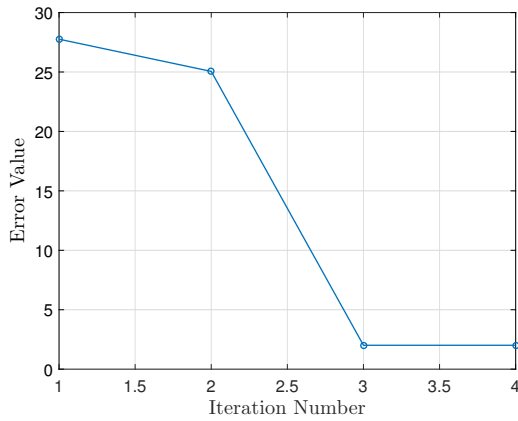


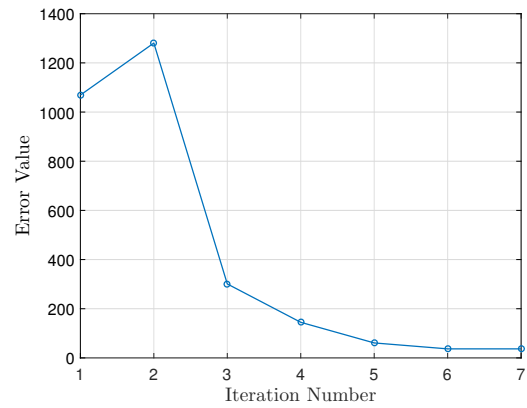
Figure 4.9: Measured voltage to ground of magnet 10 for the time window including the time where the FPA, the EE1, the EE2 and the short occurred. The peaks of the derivative of the signal indicate the times where the 3 events occur.

The measured voltage to ground signal of magnet 10 as well as the numerical derivative of the signal are presented in figure 4.9, from which t_{FPA} can be found by identifying the peaks. In figure 4.8, the similarities between the plots of the different magnets can be seen for the regions where fast transients occur. Therefore, it is true that the numerical derivative of the voltage to ground signal of any magnet can be used in order to find the time values of t_{FPA} and t_{SHORT} . The first 3 peaks with the highest amplitude value reveal the times when the 3 events of the FPA occurred. Since the numerical derivative is calculated as the difference between adjacent points, it is important to define the previous time point as the time the event occurs, rather than the point where the peak is located at. Hence, looking at figure 4.9 it becomes clear that the first event of the FPA occurred at time $t = 0$, since the first peak is seen at the following data point. A fourth peak is observed at approximately 1.42s and since the previous time point needs to be considered, the time of the short occurrence is defined as $t_{SHORT} = 1.4s$. It should be mentioned that although the time axis in the plots has already been shifted so that the FPA occurs at 0s, mainly in order to keep the plots uniform, this can only be achieved after the time of its occurrence has first been determined using the method described above.

For the measured signal of the circuit current, the time when the FPA occurs can be found by obtaining the datapoint when it reaches its peak value. In figure 3.4, it has been shown that the current is initially ramped up to a maximum value, after which it shortly reaches a plateau and starts decaying almost exponentially following the opening of the EE2 switch. The obtained signals for the current in the circuit can also be shifted



(a) Error value as function of iteration number when ℓ^1 -Norm is used as metric.



(b) Error value as function of iteration number when ℓ^2 -Norm is used as metric.

Figure 4.10: Error value as function of iteration number for the cases that the error is calculated using the ℓ^1 -Norm and ℓ^2 -Norm.

so that $t_{FPA} = 0$ s, which leads to their synchronisation with the measured voltage to ground signals.

The next step followed by the algorithm is the optimisation of the values of R_{EE1} and R_{EE2} to better match the ones in the circuit where the measured data were obtained. The algorithm picks a time point of about 1.2s after the FPA, which follows the openings of both EE resistors and precedes the fault occurrence. The initial values that are provided to the optimisation function are the nominal values of the EE resistors, which for the LHC main dipole circuit have values of $R_{EE} = 71$ m Ω . The algorithm achieves convergence to the optimised values of $R_{EE1} = 70.2$ m Ω and $R_{EE2} = 68.4$ m Ω in 3 iterations, as seen in figure 4.10a, when the total error is calculated as presented in equation 4.19. In figure 4.10b, the convergence of the objective function, when the ℓ^2 -Norm is used, can be seen, which converges slower to the same resistance values, requiring 6 iterations in total. A comparison of the measured voltages to ground, obtained using the nominal values for the resistances and the ones obtained with the optimised EE resistance values, is presented in figure 4.11. The fact that the optimised values are obtained requiring only a small number of iterations and without a major increase of the total computational time, makes the inclusion of the optimisation process in the algorithm beneficial, since a better match with the circuit values is achieved.

With all the required input parameters and the optimised resistance values, the algorithm solves the system of differential equations and computes the analytical solution for the current in the circuit as well as the current through the short. For the differential equations to be solved symbolically, a total time of about 1.6s is required. The computational time needed for the values of the solutions of the currents to be found, from which the voltages to ground are calculated, depends on the total number of points of the time vector substituted in the analytical expressions. It would be a logical step for the algorithm to compute the value of the currents for the part of the measured signal time vector starting from a specified point after the short and ending at a time when all

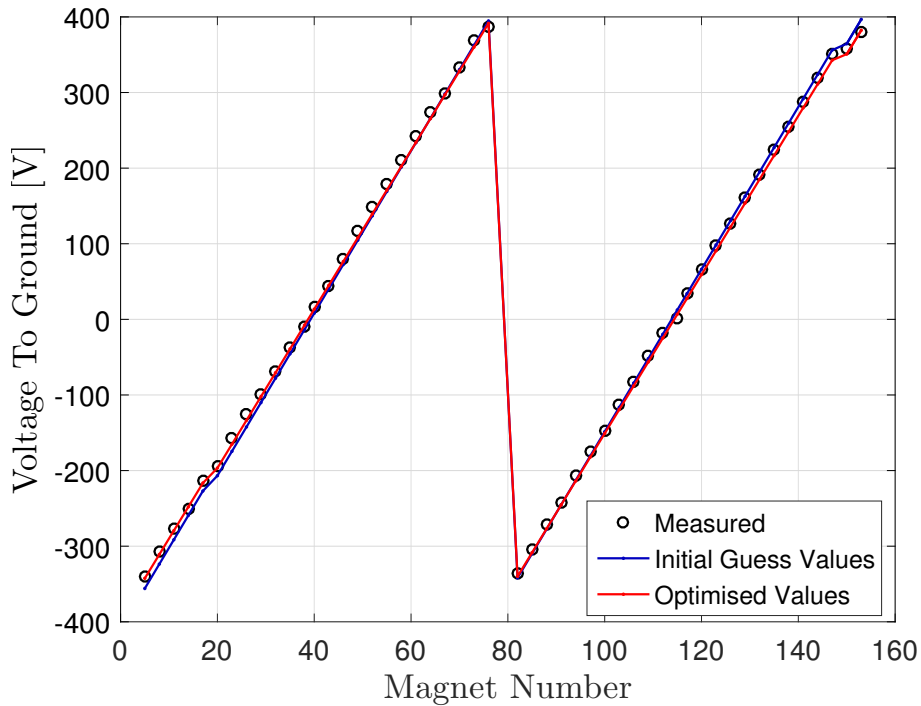


Figure 4.11: Comparison of voltage to ground values over for all magnet positions with the nominal and the optimised R_{EE} values.

the measured signals have decayed to zero. For the specific case study, the part of the total vector containing these values has a length of 2630 discrete time points.

A comparison of the time required for the calculation of the voltage to ground values for different time vector lengths is shown in table 4.3. Firstly, it can be observed that the time needed for the calculation of the differential equation solutions remains the same regardless of the grid size, since symbolic variables are used in the final equations. For the calculation of the voltages to ground, it can be seen that dividing the time vector size in half, decreases the computational time also by a factor of two, with the calculation requiring 4 times less computational time when the vector has 4 times less points. However, the same proportional decrease does not follow when the length of the time grid is reduced by a factor of 10 and 100 respectively and it can be seen that calculating the voltage values at 5 individual time points, requires approximately the same computational time as a grid with 657 discrete points. Hence, a compromise has to be made regarding the length of the time vector, since achieving small values for the total computational time is essential. A vector that consists of about 200 discrete points, starting from the chosen time point following the short and up to the point where the voltages have decayed to zero, is hence preferred over individual time points. Finally, after the current values at all grid points have been calculated, there is no major advantage in computing the voltage to ground matrix only for individual time points, as can be seen from the values in the last column of the table.

A time of about 1s after the short has occurred in the circuit is chosen for the analysis to be performed. At the specified time, the current in the circuit has decayed to a value of 11.25 kA, which is considered as I_0 . Additionally, referring back to ta-

Table 4.3: Comparison of Algorithm Computational Time for Different Time Vector Sizes

Time Grid Length	Calculate Symbolic Solutions	Calculate Voltage to Ground Matrix for All Points of Time Grid	Calculate Voltage to Ground Matrix for Single Point of Time Grid
2630	1.63 s	7.1 s	6.7 s
1315	1.63 s	3.66 s	3.98 s
657	1.63 s	2.22 s	2.28 s
263	1.63 s	1.13 s	1.15 s
26	1.63 s	0.50 s	0.50 s
1	1.63 s	0.42 s	0.42 s

ble 4.2 at the specified current value, 8 more magnets have quenched, bringing the total number of quenched magnets to 12 and more specifically the ones at positions [19, 149, 150, 5, 148, 146, 147, 151, 154, 153, 152, 8]. The measured signal of the current in the circuit, obtained from the Post-Mortem system, is compared to the analytically calculated one, with the two signals plotted in figure 4.12. In the figure, it becomes clear that although the two curves show good agreement up to a current value of approximately 5 kA, they start diverging after that point with the relative difference reaching a maximum value of about 0.21 around 2 kA. It is known that in the actual circuit the time constant value of the current discharge changes over time, mainly due to the temperature increase of the EE resistors, which alters their resistance values and consequently the equivalent resistance of the circuit. At the same time, this also reveals a first limitation of the proposed reduced model and algorithm when the resistors used to solve the differential equations are defined as constants. However, with the short occurring at the current level value of 11.31 kA in this case study, a good match of the two curves is expected for a large number of time points following the short.

For the calculation of the currents and the voltages to ground, two free parameters remain undefined in the analytical solutions, namely the resistance of the short to ground and the position at which the short occurred. The algorithm then computes the voltages to ground for resistance values at different orders of magnitude, namely $R = [0.1, 1, 10, 100, 1000] \Omega$ and the short positions for which the peak voltage values are reached, namely 1, 77, 78 and 154, as has been discussed in the theoretical description of the algorithm. For the chosen time vector, the algorithm required a total of approximately 20 s to compute the voltage to ground values for all chosen parameters.

For the signals of the specific event, small distance values are obtained for short resistances $R_s = 0.1 \Omega$ and $R_s = 1 \Omega$, with the distance increasing for higher resistance values. Graphically this is presented in figures 4.13 and 4.14. It can be seen that in the case of the higher resistance, shown in figure 4.14, the curve of the measured voltage values deviates from the voltage distributions of the extreme cases and consequently the ones for shorts occurring at the rest of the magnet positions, that fall in between the

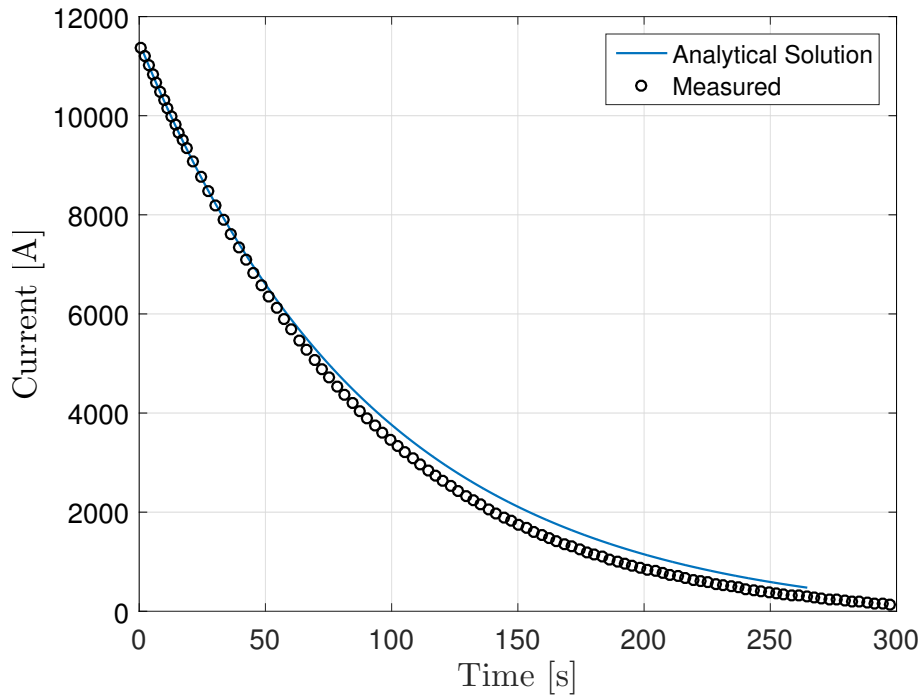


Figure 4.12: Comparison of the measured circuit current with the analytically calculated values.

extreme ones. On the other hand, for resistance $R_s = 0.1 \Omega$ a good fit is observed, with the measured voltages even obtaining smaller values than those with a short at position 77. For a resistance value of $R_s = 1 \Omega$, a close fit was also achieved, with it being the next value larger than resistance $R_s = 0.1 \Omega$, for which the voltages were calculated. The algorithm hence identifies that the short to ground in the circuit, obtained a resistance in the range of 0.1 to 1Ω .

The accuracy of the results provided by the algorithm can be verified, since the value of the short resistance that appeared in the circuit was measured following the event and a value of about 0.4Ω was reported. The algorithm has hence correctly identified that the short resistance in the circuit obtains a low value, which is included in the range, that was provided as output. The low value calculated by the algorithm for the short, also reveals that at the chosen point in time, the fuse in the circuit has not blown up.

Having obtained a range of values for the short resistance for which good accordance is achieved between the measured and analytically calculated signals, the last free variable is the magnet position where the short occurred. Since a good fit was achieved with a value of 0.1Ω for the resistance, the voltage to ground values for every magnet are calculated for all 154 short positions. With the solutions of the differential equations already computed, this requires approximately 150s for the chosen time vector of about 200 points. The distance between the voltage to ground values for each case is computed using the formula in equation 4.21.

The 10 smallest distance values that were computed, as well as the corresponding short positions, are presented in table 4.4 and the voltages to ground for each of the measured magnets are plotted in figure 4.15. It can be seen that most magnets in the positions shown in table 4.4 have already quenched at the time the short occurred. This

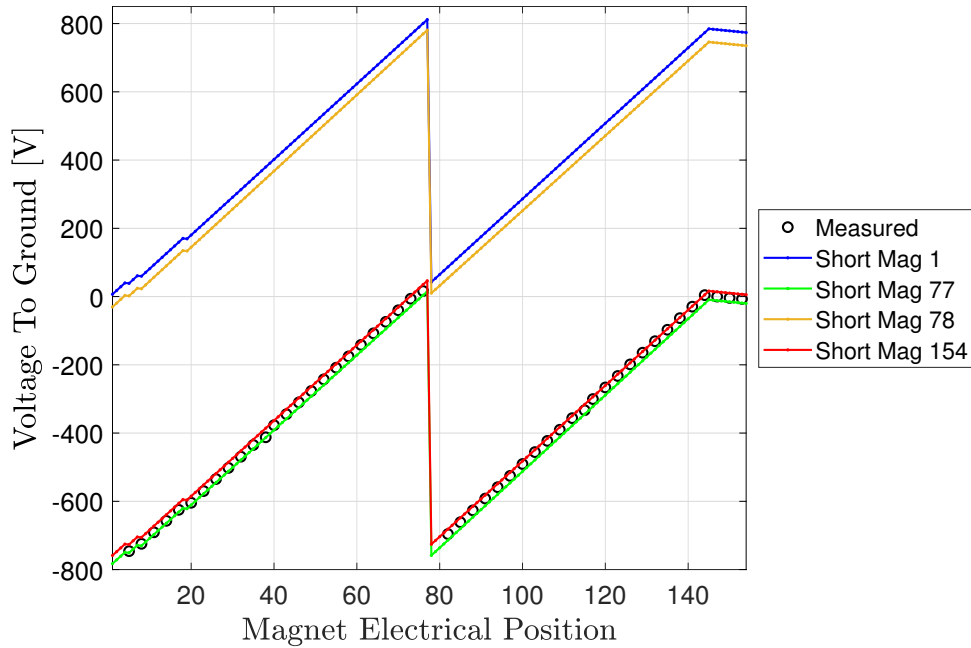


Figure 4.13: Measured and analytically calculated voltage distributions for short to ground occurring at different magnet electrical positions with a short resistance $R_s = 0.1\Omega$. The distance of the measured curve from the analytically calculated ones is used to define the range in which the short resistance belongs.

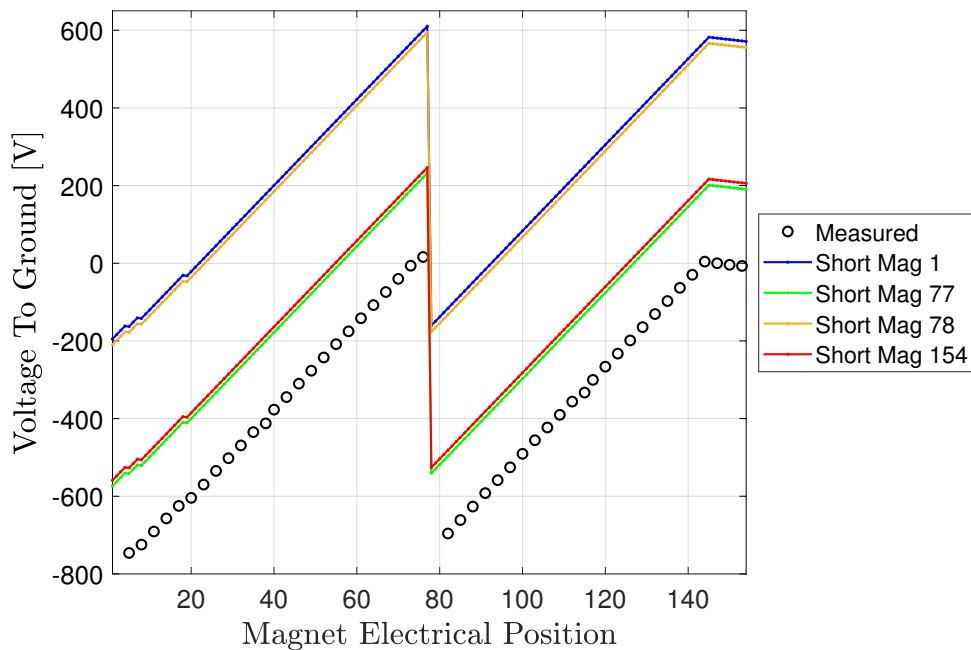


Figure 4.14: Measured and analytically calculated curves for short to ground occurring at different magnet electrical positions with a short resistance $R_s = 10\Omega$.

means that for those magnets at the time of the short, the voltage difference between two consecutive magnets is equal to 1.2V instead of the value of approximately 11.1V that is seen for the non-quenched magnets in the chain. Since it is also known that an error exists in the calculated values of the current in the circuit, when compared to the measured ones, it would not be correct for the algorithm to claim that the short occurred

Table 4.4: Smallest Mean Absolute Distance Values Achieved for a Resistance of $0.1\ \Omega$ and Short Positions Where They Occurred

Short Position	Distance [V]
146	5.44
147	5.93
75	6.02
149	6.70
150	7.24
148	8.32
151	8.51
76	9.23
152	9.82
153	10.07

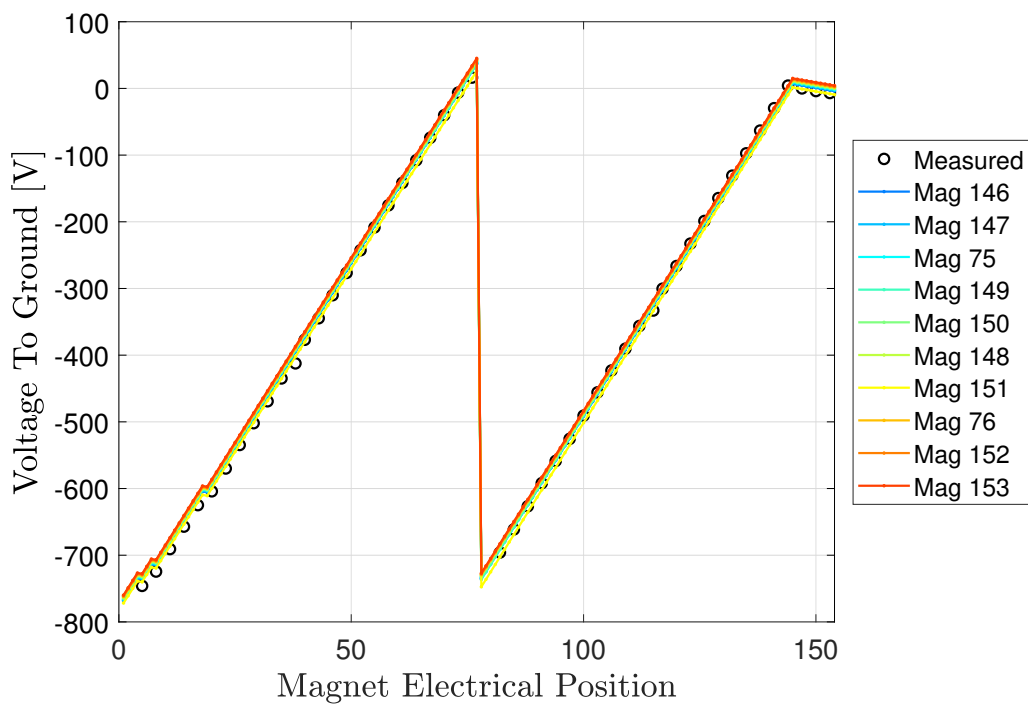


Figure 4.15: Comparison of measured voltage to ground distribution and the analytically calculated ones for different short positions with a short resistance of $R_s = 0.1\ \Omega$.

in the short position with the smallest distance. Instead, a list of the possible positions with the highest probability is returned. With knowledge that the short position occurred at magnet 149, it is seen that the algorithm includes the correct short position in the range of possible values that it provides as output, despite the fact that it is not the one for which the minimum distance value was obtained.

4.5 Discussion and Future Work

To conclude, the first test of the algorithm using measured data as input shows promising results. For the analysed short to ground event, the fact that all magnets after position 146 had already quenched, led to a large number of voltage distributions obtaining small distance values when compared to the measured voltages and could all be characterised as possible solutions. Despite this fact, the algorithm successfully identified the range of the short resistance, that includes the accurate value known from onsite measurements. The algorithm also narrowed the possible short positions down to 10 magnets, with the actual short position included in the range. This information required a total time of about 250 s to be provided, after the measured data had been given as input, which is significantly faster than the total computational time that numerical simulations would need to complete.

A first test of the algorithm has been performed in this thesis. Considering the promising results, further testing is deemed necessary using measurement data from different short to ground events. For the event analysed in this work, the magnet at which the short occurred, had quenched before the appearance of the short. Additionally, this was also the case for the magnets directly following and preceding the short position. It would be interesting hence to test the algorithm using an event for which the magnet where the short occurs is not quenched and observe whether a smaller range of possible short positions can be identified by the algorithm, due to larger deviations between the final distance values. It has been described that the algorithm reaches a conclusion regarding the position where the short occurred by calculating the voltage to ground values at a specific time instance. It would be of interest to investigate whether and by how much the results provided by the algorithm change, when a time point belonging in the range where larger relative error values are obtained is provided. The larger deviations that were observed between the measured and analytically calculated values of the circuit current after a certain time following the short, could be reduced by specifying the equivalent circuit resistance as a function of time instead of a constant value. Finally, by further reducing the time that is needed for computing the result of the symbolic solutions for the currents in the circuit, the algorithm could be run online. In this case, the results would be computed at timed intervals only a few seconds apart, meaning that information about the short could become available even more quickly.

CHAPTER 5

CONCLUSION

The LHC main dipole circuit consists of 8 sectors, each including 154 superconducting main bending dipole magnets. During normal operation, the current in the circuit is ramped up to a nominal value after which it reaches a plateau, with the voltages to ground values of the magnets following the same behaviour. In the event that a short to ground occurs in the circuit, a fast power abort is triggered which is followed by the opening of two switches inserting two energy extraction resistors in the circuit, over which large voltage drops occur.

The first focus point of this thesis has been the analysis of the LHC main dipole circuit, in order for the worst cases to be identified for different parameters of the short to ground. After obtaining a better understanding of the circuit behaviour when a short occurs, an algorithm able to provide information on a short circuit that occurred has also been developed and tested.

In chapter 2, a general introduction to the models of the LHC main dipole circuit which are used to perform numerical simulations has been provided. A description of the events occurring during a fast power abort, which is triggered when a short exists in the circuit, has been detailed. A brief analysis of the circuit behaviour and more specifically the voltages to ground obtained by the magnets at different electrical positions during a fast power abort has also been provided.

In chapter 3 a short to ground has been modeled and its effect on the circuit and more specifically the voltage to ground values of different magnets has been analysed. The blow-up behaviour of the fuse that exists in the grounding lines of the circuit has been discussed, which when included in the circuit simulations, increases the accuracy of the model for the case where a short to ground has occurred. A simulation scheme has been proposed in order to achieve the modeling of the fuse behaviour, which consists of a common interface that combines *PSpice* simulations and numerical calculations in *MATLAB*. The results of the simulations after performing a parametric sweep of the short position and the short resistance value have been presented. The chapter concludes with

the identification of the extreme voltage to ground values that can appear at magnets for different combinations of short resistances and positions, providing therefore the answer to the first research question of the thesis. A worst-case voltage to ground peak value of 1.9 kV has been determined for the circuit, which can occur at magnet positions 57-77 and 78-98 in the cases where the fuse blows up and the resistance of the short has a value less than or equal to $10\ \Omega$. For cases where the short to ground resistance has a value larger than $10\ \Omega$, the voltages to ground reach lower values.

In chapter 4, an algorithm able to provide information concerning a single short to ground that occurred in the LHC main dipole circuit has been proposed and both the second and third research questions of the thesis have been addressed. A simplified model of the LHC main dipole circuit, accurate for short transients and which reproduces the behaviour of the circuit under the existence of a single short to ground, is used by the algorithm in order to provide information about the short. The differential equations of the simplified model, from which the voltages to ground are analytically calculated, have been successfully derived and solved. During this process, a limitation has been revealed due to the fact that the discharge time constant of the circuit varies with respect to time, which reduces the accuracy of the algorithm for certain time points following the short. At the same time however, this error reaches a value of about 17%, which can be considered relatively small, since in the reduced model of the accelerator circuit all nonlinear effects are ignored and only resistive and inductive elements are used. The algorithm has been tested using measured signal data from a short circuit to ground event that occurred in the circuit. The algorithm determined the 10 magnet positions where the short to ground most likely occurred, which correctly included its actual position in the circuit. Regarding the short resistance, the algorithm specified a range of possible values, which correctly included the value of the short resistance that appeared in the circuit during the short to ground event. Finally, with the reduction of the main dipole circuit to an equivalent circuit model consisting solely of resistive and inductive elements, the values of which are programmatically calculated, it becomes possible to apply the algorithm to other accelerator circuits by simply changing its input parameters.

BIBLIOGRAPHY

- [1] “The Large Hadron Collider”, Accessed 20 Dec, 2018. [Online]. Available: <https://home.cern/science/accelerators/large-hadron-collider>.
- [2] *LHC the guide*, Accessed 15 Jan, 2019. [Online]. Available: <https://project-physicsteaching.web.cern.ch/project-physicsteaching/english/brochures/lhc-guide.pdf>.
- [3] “Interim Summary Report On The Analysis Of The 19 September 2008 Incident At The LHC”, Tech. Rep., 2008.
- [4] M. Bajko, and 30 co-authors, “REPORT OF THE TASK FORCE ON THE INCIDENT OF 19 SEPTEMBER 2008 AT THE LHC”, Tech. Rep., 2011.
- [5] “The Development of the Control System for the Cryogenics in the LHC Tunnel”, Tech. Rep., Accessed 20 Nov, 2018. [Online]. Available: https://www.researchgate.net/figure/Layout-of-8-LHC-sectors-RF-and-main-detectors_fig1_254467777.
- [6] “LHC experiments”, Accessed 7 Dec, 2018. [Online]. Available: <https://home.cern/science/experiments>.
- [7] J. Bardeen, L. N. Cooper, and J. R. Schrieffer, “Theory of superconductivity”, *Phys. Rev.*, vol. 108, pp. 1175–1204, 5 Dec. 1957. DOI: 10.1103/PhysRev.108.1175.
- [8] O. S. Brüning, P. Collier, P. Lebrun, S. Myers, R. Ostojic, J. Poole, and P. Proudlock, *LHC Design Report*, ser. CERN Yellow Reports: Monographs. Geneva: CERN, 2004. [Online]. Available: <https://cds.cern.ch/record/782076>.
- [9] N. Andreev, K. Artoos, L. Bottura, F. Rodriguez-Mateos, S. Russenschuck, N. Siegel, A. Siemko, F. Sonnemann, D. Tommasini, and I. Vanenkov, “PERFORMANCE OF FIVE AND SIX BLOCK COIL GEOMETRIES IN SHORT SUPERCONDUCTING DIPOLE MODELS FOR THE LHC”, CERN, Geneva, Switzerland, 1999.
- [10] L. Rossi, “The LHC Superconducting Magnets”, 2003.

-
- [11] “The LHC cryogenic system”, Accessed 7 Jan, 2019. [Online]. Available: <http://lhc-machine-outreach.web.cern.ch/LHC-machine-outreach/components/doc/TheLHCcryogenicsystem.pdf>.
- [12] E. Ravaioli, “CLIQ. A new quench protection technology for superconducting magnets”, English, PhD thesis, University of Twente, Jun. 2015, ISBN: 978-90-365-3908-1. DOI: 10.3990/1.9789036529081.
- [13] F. Rodriguez-Mateos, P. Pugnati, S. Sanfilippo, R. Schmidt, A. Siemko, F. Sonnemann, “QUENCH HEATER EXPERIMENTS ON THE LHC MAIN SUPERCONDUCTING MAGNETS”, Tech. Rep., 2000.
- [14] R. Denz, “QUENCH PROTECTION SYSTEM”, CERN, Geneva, Switzerland, Tech. Rep.
- [15] E. Ciapala, F. Rodríguez-Mateos, R. Schmidt, and J. Wenninger, “The LHC Post-mortem System”, CERN, Geneva, Tech. Rep. LHC-PROJECT-NOTE-303, Oct. 2002. [Online]. Available: <http://cds.cern.ch/record/691828>.
- [16] “MB Training campaign 2016, December 2016”,
- [17] “Simulation of Transient Effects in Accelerator Magnets”, Accessed 20 Nov, 2018. [Online]. Available: https://espace.cern.ch/steam/_layouts/15/start.aspx#/SitePages/Home.aspx.
- [18] “TE-MPE Group Page, Machine Protection and Electrical Integrity Group, Technology Department, CERN”, Accessed 20 Nov, 2018. [Online]. Available: <https://mpe.web.cern.ch/content/structure/mpe-pe>.
- [19] E. Ravaioli, K. Dahlerup-Petersen, F. Formenti, J. Steckert, H. Thiesen, and A. Verweij, “Modeling of the voltage waves in the LHC main dipole circuits”, Tech. Rep., 2011.
- [20] E. Ravaioli, K. Dahlerup-Petersen, F. Formenti, V. Montabonnet, M. Pojer, R. Schmidt, A. Siemko, M. S. Camillocci, J. Steckert, H. Thiesen, and A. Verweij, “Impact of the Voltage Transients After a Fast Power Abort on the Quench Detection System in the LHC Main Dipole Chain”, *IEEE Transactions on Applied Superconductivity*, Jun. 2012, ISSN: 1051-8223. DOI: 10.1109/TASC.2012.2183572.
- [21] “FPAinRB, Special FPA tests at +10 A/s with read-out of all iQPS buffers”, Accessed 17 Dec, 2018. [Online]. Available: <https://twiki.cern.ch/twiki/bin/viewauth/MP3/FPAinRB>.
- [22] “Matlab Documentation: jet”, Accessed 7 Jan, 2019. [Online]. Available: <https://www.mathworks.com/help/matlab/ref/jet.html>.
- [23] A. E. Kennelly, “The equivalence of triangles and three-pointed stars in conducting networks”, *Electrical World and Engineer*, vol. 34, pp. 413–414, 1899.
- [24] R. Billen; M. Marczukajtis, M. Peryt, “THE LHC LOGGING”, CERN, Geneva, Tech. Rep., Sep. 2002. [Online]. Available: <https://edms.cern.ch/ui/#!master/navigator/document?D:1488667908:1488667908:subDocs>.

BIBLIOGRAPHY

- [25] “DQLPUS related magnets S34”, Accessed 20 Jan, 2019. [Online]. Available: <https://wikis.cern.ch/display/MPEEP/DQLPUS+related+magnets+S34>.
- [26] T. J. Ypma, “Historical development of the newton-raphson method”, *SIAM Review*, vol. 37, pp. 531–551, 1995.
- [27] R. A. Horn and C. R. Johnson, *Norms for Vectors and Matrices*. Cambridge, England: Cambridge University Press, 1990, ch. 5.
- [28] M. Prioli, M. Maciejewski, L. Bortot, A. Verweij, *Circuit simulations of the fault to ground in sector 34 on 8/12/2016*, 2016.
- [29] M. Bednarek, “RB.A34 Short To Ground Report”, CERN, Geneva, Tech. Rep., 2016. [Online]. Available: <https://edms.cern.ch/ui/#!/master/navigator/document?D:1488667908:1488667908:subDocs>.
- [30] “Earth fault 8 Dec 2016 ”, Accessed 10 Jan, 2019. [Online]. Available: <https://twiki.cern.ch/twiki/bin/view/MP3/RBA34earthfailure>.
- [31] E. Ravaioli, B. Auchmann, M. Bednarek, Z. Charifoulline, J. Ludwin, and A. Verweij, “Analysis and Simulation of the event in RB.56 on the 9 February 2015”, Tech. Rep., 2015.
- [32] E. Ravaioli, “Advanced simulations of events in the RB circuit”, Tech. Rep., 2011.

APPENDIX A

APPENDIX

A.1 Wye-Delta Transform

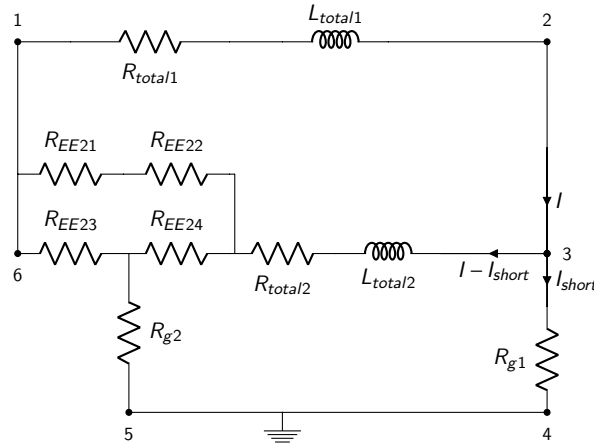
The Wye-Delta transform is used in order to simplify the resistor branch that models the second energy extractor of the circuit, namely [Energy Extraction 2 \(EE2\)](#). In this section of the Appendix, an analytic derivation of the equivalent resistances R_1 , R_2 , R_3 included in the circuit of [figure A.1b](#) as a function of the resistors R_{EE21} , R_{EE22} , R_{EE23} and R_{EE24} of the configuration shown in [figure A.1a](#) is detailed. The derived equivalent resistances are used to calculate the values of resistances R_{bf}, R_{af} and inductances L_{bf}, L_{af} of the lumped circuit of [figure A.1c](#).

$$R_{total} = R_{EE23} + R_{EE24} + (R_{EE22} + R_{EE21}) \quad (\text{A.1})$$

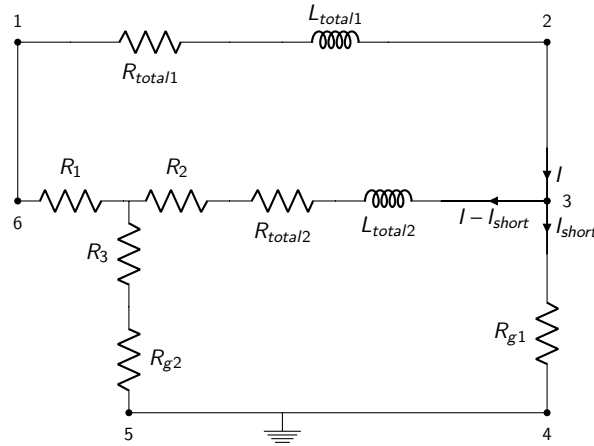
$$R_1 = \frac{R_{EE23}(R_{EE22} + R_{EE21})}{R_{total}} \quad (\text{A.2})$$

$$R_2 = \frac{R_{EE24}(R_{EE22} + R_{EE21})}{R_{total}} \quad (\text{A.3})$$

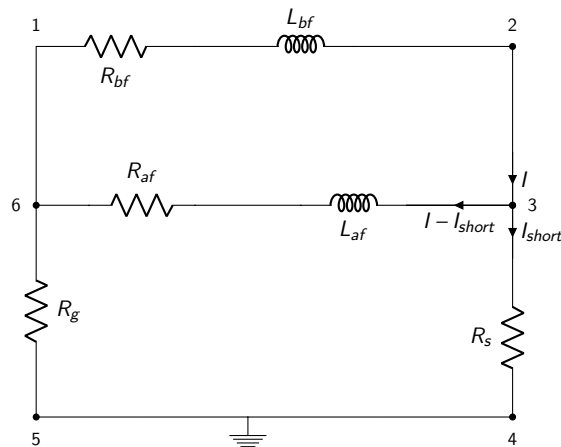
$$R_3 = \frac{R_{EE24}R_{EE23}}{R_{total}} \quad (\text{A.4})$$



(a) Reduced circuit of the LHC main dipole circuit for the case when a short to ground has occurred.



(b) Wye-Delta transform applied to circuit.



(c) Final circuit simplification with minimum number of parameters.

Figure A.1: Stages of equivalent circuit transformation of the initial circuit (top) to the final simplified LHC circuit diagram (bottom) using the Wye-Delta Transform.

A.2 LHC Magnet Crate Layout

1_Pin	2_Pin	3_Pin
1	154	
2	153	
3	152	
4	151	
5	150	6
149	7	148
8	147	9
146	10	145
11	144	12
143	13	142
14	141	15
140	16	139
17	138	18
137	19	136
20	135	21
134	22	133
23	132	24
131	25	130
26	129	27
128	28	127
29	126	30
125	31	124
32	123	33
122	34	121
35	120	36
119	37	118
38	117	39
116	40	115
41	114	42
113	43	112
44	111	45
110	46	109
47	108	48
107	49	106
50	105	51
104	52	103
53	102	54
101	55	100
56	99	57
98	58	97
59	96	60
95	61	94
62	93	63
92	64	91
65	90	66
89	67	88
68	87	69
86	70	85
71	84	72
83	73	82
74	81	
75	80	
76	79	
77	78	

Figure A.2: Electrical position of magnets included in crates 1 to 54 crates, listed from smallest to highest crate number.

A.3 Complete Expressions of Circuit Currents Analytical Solutions

The solutions for currents I and I_{SHORT} that are obtained by analytically solving the differential equations 4.9 and 4.10 are presented in figure A.3. The equations also contain 42 σ parameters which are a function of the elements of circuit 4.3 and are presented in figure A.4 and A.5 respectively.

A.4 GitLab Repository

The *MATLAB* scripts and the netlist models that were used for the simulation scheme of the fuse blow-up behaviour, as well as to perform the parametric analysis for different short positions and resistance values can be found in the *Fault Analysis* repository on the *STEAM* GitLab page. The short circuit algorithm described in the second part of the thesis is also included in the repository. The link is provided below. It should be mentioned however, that a CERN account is required to access the repository.

<https://gitlab.cern.ch/steam/fault-analysis>

$$\begin{aligned}
\mathbf{I} = & -e^{-\frac{t\sigma_{35}}{2\text{LafLbf}}} \left(\frac{\sigma_{34} - \sigma_{33} - \text{Laf Quenchedbf } \sigma_{42} + \text{Lbf Quenchedaf } \sigma_{42} - \sigma_{22} + \sigma_{21} + \sigma_{20} - \sigma_{19} + \sigma_{18} - \sigma_{17} - I_0 \text{Laf Rbf } \sigma_{42} +}{\sigma_{35} \sigma_{42}} \right. \\
& + \frac{I_0 \text{Lbf Raf } \sigma_{42} - \text{Laf Lbf Quenchedbf Raf} + \text{Laf Lbf Quenchedaf Rbf} - \text{Laf Lbf Quenchedaf Rg} + \text{Laf Lbf Quenchedbf Rg} -}{\sigma_{35} \sigma_{42}} \\
& - \frac{\text{Laf Lbf Quenchedaf Rs} + \text{Laf Lbf Quenchedbf Rs} + \sigma_{16} - \sigma_{15} + \sigma_{14} - \sigma_{13} - \sigma_{26} + \sigma_{25} - \sigma_{24} + \sigma_{23} +}{\sigma_{35} \sigma_{42}} + \\
& \left. + \frac{e^{\sigma_{32} + \sigma_{31} + \sigma_{30} + \sigma_{29} + \sigma_{28} + \sigma_{27} - \sigma_{40}} (\sigma_6 - \sigma_5 + \sigma_4 - \sigma_3 + \sigma_2 - \sigma_1 - \sigma_{39} + \sigma_{38} + \sigma_{12} - \sigma_{11} + \sigma_{10} - \sigma_9 + \sigma_8 - \sigma_7)}{2 \text{Laf Lbf} (\text{Rg} (\text{Laf} + \text{Lbf}) - \sigma_{42} + \text{Rs} (\text{Laf} + \text{Lbf}) + \text{Laf Rbf} + \text{Lbf Raf}) \sigma_{42}} \right) + \\
\left(\frac{\sigma_{35}}{2 \sigma_{41}} - \sigma_{37} \right) - e^{-\frac{t\sigma_{36}}{2\text{LafLbf}}} & \left(\frac{\sigma_{34} - \sigma_{33} + \text{Laf Quenchedbf } \sigma_{42} - \text{Lbf Quenchedaf } \sigma_{42} - \sigma_{22} + \sigma_{21} + \sigma_{20} - \sigma_{19} + \sigma_{18} - \sigma_{17} +}{\sigma_{36} \sigma_{42}} \right. \\
& + \frac{I_0 \text{Laf Rbf } \sigma_{42} - I_0 \text{Lbf Raf } \sigma_{42} - \text{Laf Lbf Quenchedbf Raf} + \text{Laf Lbf Quenchedaf Rbf} - \text{Laf Lbf Quenchedaf Rg} +}{\sigma_{36} \sigma_{42}} \\
& + \frac{\text{Laf Lbf Quenchedbf Rg} - \text{Laf Lbf Quenchedaf Rs} + \text{Laf Lbf Quenchedbf Rs} + \sigma_{16} - \sigma_{15} + \sigma_{14} - \sigma_{13} - \sigma_{26} + \sigma_{25} - \sigma_{24} + \sigma_{23} +}{\sigma_{36} \sigma_{42}} + \\
& \left. + \frac{e^{\sigma_{32} + \sigma_{31} + \sigma_{30} + \sigma_{29} + \sigma_{28} + \sigma_{27} + \sigma_{40}} (\sigma_6 - \sigma_5 + \sigma_4 - \sigma_3 + \sigma_2 - \sigma_1 + \sigma_{39} - \sigma_{38} + \sigma_{12} - \sigma_{11} + \sigma_{10} - \sigma_9 + \sigma_8 - \sigma_7)}{2 \text{Laf Lbf} (\sigma_{42} + \text{Rg} (\text{Laf} + \text{Lbf}) + \text{Rs} (\text{Laf} + \text{Lbf}) + \text{Laf Rbf} + \text{Lbf Raf}) \sigma_{42}} \right) \left(\sigma_{37} - \frac{\sigma_{36}}{2 \sigma_{41}} \right) \\
\mathbf{I}_{\text{short}} = & e^{-\frac{t\sigma_{36}}{2\text{LafLbf}}} \left(\frac{\sigma_{34} - \sigma_{33} + \text{Laf Quenchedbf } \sigma_{40} - \text{Lbf Quenchedaf } \sigma_{40} - \sigma_{22} + \sigma_{21} + \sigma_{20} - \sigma_{19} + \sigma_{18} - \sigma_{17}}{\sigma_{36} \sigma_{40}} \right. \\
& + \frac{I_0 \text{Laf Rbf } \sigma_{40} - \text{Laf Lbf Quenchedbf Raf} + \text{Laf Lbf Quenchedaf Rbf} - \text{Laf Lbf Quenchedaf Rg} + \text{Laf Lbf Quenchedbf Rg} -}{\sigma_{36} \sigma_{40}} \\
& - \frac{\text{Laf Lbf Quenchedaf Rs} + \text{Laf Lbf Quenchedbf Rs} + \sigma_{16} - \sigma_{15} + \sigma_{14} - \sigma_{13} - \sigma_{26} + \sigma_{25} - \sigma_{24} + \sigma_{23} +}{2 \text{Laf Lbf} (\sigma_{40} + \text{Rg} (\text{Laf} + \text{Lbf}) + \text{Rs} (\text{Laf} + \text{Lbf}) + \text{Laf Rbf} + \text{Lbf Raf}) \sigma_{40}} + \\
& \left. + \frac{e^{\sigma_{32} + \sigma_{31} + \sigma_{30} + \sigma_{29} + \sigma_{28} + \sigma_{27} + \sigma_{39}} (\sigma_6 - \sigma_5 + \sigma_4 - \sigma_3 + \sigma_2 - \sigma_1 + \sigma_{38} - \sigma_{37} + \sigma_{12} - \sigma_{11} + \sigma_{10} - \sigma_9 + \sigma_8 - \sigma_7)}{2 \text{Laf Lbf} (\sigma_{40} + \text{Rg} (\text{Laf} + \text{Lbf}) + \text{Rs} (\text{Laf} + \text{Lbf}) + \text{Laf Rbf} + \text{Lbf Raf}) \sigma_{40}} \right) - \\
& - e^{-\frac{t\sigma_{35}}{2\text{LafLbf}}} \left(\frac{\sigma_{34} - \sigma_{33} - \text{Laf Quenchedbf } \sigma_{40} + \text{Lbf Quenchedaf } \sigma_{40} - \sigma_{22} + \sigma_{21} + \sigma_{20} - \sigma_{19} + \sigma_{18} - \sigma_{17} -}{\sigma_{35} \sigma_{40}} \right. \\
& - \frac{I_0 \text{Laf Rbf } \sigma_{40} + I_0 \text{Lbf Raf } \sigma_{40} - \text{Laf Lbf Quenchedbf Raf} + \text{Laf Lbf Quenchedaf Rbf} - \text{Laf Lbf Quenchedaf Rg} +}{\sigma_{35} \sigma_{40}} \\
& + \frac{\text{Laf Lbf Quenchedbf Rg} - \text{Laf Lbf Quenchedaf Rs} + \text{Laf Lbf Quenchedbf Rs} + \sigma_{16} - \sigma_{15} + \sigma_{14} - \sigma_{13} - \sigma_{26} + \sigma_{25} - \sigma_{24} + \sigma_{23} +}{\sigma_{35} \sigma_{40}} + \\
& \left. + \frac{e^{\sigma_{32} + \sigma_{31} + \sigma_{30} + \sigma_{29} + \sigma_{28} + \sigma_{27} - \sigma_{39}} (\sigma_6 - \sigma_5 + \sigma_4 - \sigma_3 + \sigma_2 - \sigma_1 - \sigma_{38} + \sigma_{37} + \sigma_{12} - \sigma_{11} + \sigma_{10} - \sigma_9 + \sigma_8 - \sigma_7)}{2 \text{Laf Lbf} (\text{Rg} (\text{Laf} + \text{Lbf}) - \sigma_{40} + \text{Rs} (\text{Laf} + \text{Lbf}) + \text{Laf Rbf} + \text{Lbf Raf}) \sigma_{40}} \right)
\end{aligned}$$

Figure A.3: Analytical solution of current I and I_{short} in the simplified circuit of figure 4.3.

$$\begin{aligned}
 \sigma_1 &= 2 \text{Laf}^2 \text{Lbf}^2 \text{Quenchedbf Rs} & \sigma_{19} &= \text{Lbf}^2 \text{Quenchedaf Rg} \\
 \sigma_2 &= 2 \text{Laf}^2 \text{Lbf}^2 \text{Quenchedaf Rs} & \sigma_{20} &= \text{Laf}^2 \text{Quenchedbf Rg} \\
 \sigma_3 &= 2 \text{Laf}^2 \text{Lbf}^2 \text{Quenchedbf Rg} & \sigma_{21} &= \text{Laf}^2 \text{Quenchedbf Rbf} \\
 \sigma_4 &= 2 \text{Laf}^2 \text{Lbf}^2 \text{Quenchedaf Rg} & \sigma_{22} &= \text{Lbf}^2 \text{Quenchedaf Raf} \\
 \sigma_5 &= 2 \text{Laf}^2 \text{Lbf}^2 \text{Quenchedaf Rbf} & \sigma_{23} &= I_0 \text{Laf Lbf Rbf Rs} \\
 \sigma_6 &= 2 \text{Laf}^2 \text{Lbf}^2 \text{Quenchedbf Raf} & \sigma_{24} &= I_0 \text{Laf Lbf Raf Rs} \\
 \sigma_7 &= 2 \text{Laf}^3 \text{Lbf} \text{Quenchedbf Rs} & \sigma_{25} &= I_0 \text{Laf Lbf Rbf Rg} \\
 \sigma_8 &= 2 \text{Laf} \text{Lbf}^3 \text{Quenchedaf Rs} & \sigma_{26} &= I_0 \text{Laf Lbf Raf Rg} \\
 \sigma_9 &= 2 \text{Laf}^3 \text{Lbf} \text{Quenchedbf Rg} & \sigma_{27} &= \frac{\text{Rs } t}{2 \text{Lbf}} \\
 \sigma_{10} &= 2 \text{Laf} \text{Lbf}^3 \text{Quenchedaf Rg} & \sigma_{28} &= \frac{\text{Rs } t}{2 \text{Laf}} \\
 \sigma_{11} &= 2 \text{Laf}^3 \text{Lbf} \text{Quenchedbf Rbf} & \sigma_{29} &= \frac{\text{Rg } t}{2 \text{Lbf}} \\
 \sigma_{12} &= 2 \text{Laf} \text{Lbf}^3 \text{Quenchedaf Raf} & \sigma_{30} &= \frac{\text{Rg } t}{2 \text{Laf}} \\
 \sigma_{13} &= I_0 \text{Lbf}^2 \text{Raf Rs} & \sigma_{31} &= \frac{\text{Rbf } t}{2 \text{Lbf}} \\
 \sigma_{14} &= I_0 \text{Laf Lbf Raf Rs} & \sigma_{32} &= \frac{\text{Raf } t}{2 \text{Laf}} \\
 \sigma_{15} &= I_0 \text{Laf Lbf Rbf Rg} & \sigma_{33} &= I_0 \text{Lbf}^2 \text{Raf}^2 \\
 \sigma_{16} &= I_0 \text{Laf}^2 \text{Rbf Rg} & \sigma_{34} &= I_0 \text{Laf}^2 \text{Rbf}^2 \\
 \sigma_{17} &= \text{Lbf}^2 \text{Quenchedaf Rs} & & \\
 \sigma_{18} &= \text{Laf}^2 \text{Quenchedbf Rs} & &
 \end{aligned}$$

Figure A.4: Analytical expressions of parameters σ_1 to σ_{16} and σ_{18} to σ_{34} included in the solution of I and I_{short} shown in figure A.3.

$$\sigma_{35} = \text{Laf}^2 \text{Rbf} \text{Quenchedbf}$$

$$\sigma_{36} = \text{Laf} \text{Quenchedbf} + \text{Laf} \text{Quenchedaf} - \text{Laf} \text{Quenchedbf}$$

$$\sigma_{37} = \text{Laf} \text{Rbf} - \text{Lbf} \text{Raf}$$

$$\sigma_{38} = 2 \text{Laf}^2 \text{Lbf} \text{Quenchedbf} \sigma_{42}$$

$$\sigma_{39} = 2 \text{Laf} \text{Lbf}^2 \text{Quenchedaf} \sigma_{42}$$

$$\sigma_{40} = \frac{l \sigma_{42}}{2 \text{Laf} \text{Lbf}}$$

$$\sigma_{41} = \text{Laf} \text{Rbf} - \text{Lbf} \text{Raf}$$

$$\begin{aligned} \sigma_{17} = & 2 \text{Laf} \text{Lbf} (\sigma_{35} + \sigma_{34} - \sigma_{33} - \sigma_{32} + \sigma_{31} + \sigma_{30} - \sigma_{29} - \sigma_{28} + \sigma_{27} + \sigma_{26} - \sigma_{25} - \sigma_{24} \\ & - \text{Laf} \text{Lbf} \text{Raf} \text{Quenchedbf} - \text{Laf} \text{Lbf} \text{Raf} \text{Quenchedaf} + \text{Laf} \text{Lbf} \text{Raf} \text{Quenchedaf} \\ & + \text{Laf} \text{Lbf} \text{Rbf} \text{Quenchedaf} \text{if} + \text{Laf} \text{Lbf} \text{Rg} \text{Quenchedbf} + \text{Laf} \text{Lbf} \text{Rg} \text{Quenchedbf} \\ & + \text{Laf} \text{Lbf} \text{Rg} \text{Quenchedaf} - \sigma_{23} + \text{Laf} \text{Lbf} \text{Rs} \text{Quenchedbf} + \text{Laf} \text{Lbf} \text{Rs} \text{Quenchedaf} - \sigma_{22}) \\ & - 2 \text{Laf} \text{Lbf} \sigma_{36} (\text{Laf} \text{Rbf} + \text{Lbf} \text{Raf} + \text{Laf} \text{Rg} + \text{Lbf} \text{Rg} + \text{Laf} \text{Rs} + \text{Lbf} \text{Rs}) \end{aligned}$$

$$\begin{aligned} \sigma_{42} = & \frac{\sqrt{\text{Laf}^2 \text{Rbf}^2 + 2 \text{Laf}^2 \text{Rbf} \text{Rg} + 2 \text{Laf}^2 \text{Rbf} \text{Rs} + \text{Laf}^2 \text{Rg}^2 + 2 \text{Laf}^2 \text{Rg} \text{Rs} + \text{Laf}^2 \text{Rs}^2}}{\sqrt{-2 \text{Laf} \text{Lbf} \text{Raf} \text{Rbf} - 2 \text{Laf} \text{Lbf} \text{Raf} \text{Rg} - 2 \text{Laf} \text{Lbf} \text{Raf} \text{Rs} - 2 \text{Laf} \text{Lbf} \text{Rbf} \text{Rg} - 2 \text{Laf} \text{Lbf} \text{Rbf} \text{Rs} \\ & + 2 \text{Laf} \text{Lbf} \text{Rg}^2 + 2 \text{Laf} \text{Lbf} \text{Rg}^2 + 4 \text{Laf} \text{Lbf} \text{Rg} \text{Rs} + 2 \text{Laf} \text{Lbf} \text{Rs}^2 + \text{Lbf}^2 \text{Raf}^2 + 2 \text{Lbf}^2 \text{Raf} \text{Rg} \\ & + 2 \text{Lbf}^2 \text{Raf} \text{Rs} + \text{Lbf}^2 \text{Rg}^2 + 2 \text{Lbf}^2 \text{Rg} \text{Rs} + \text{Lbf}^2 \text{Rs}^2}} \end{aligned}$$

Figure A.5: Analytical expressions of parameters σ_{35} to σ_{37} , σ_{41} and σ_{42} included in the solution of l and l_{SHORT} shown in figure A.3.